The Astrophysical Journal, 793:6 (21pp), 2014 September 20 doi:10.1088/0004-637X/793/1/6

LARGE-AMPLITUDE, CIRCULARLY POLARIZED, COMPRESSIVE, OBLIQUELY PROPAGATING ELECTROMAGNETIC PROTON CYCLOTRON WAVES THROUGHOUT THE EARTH'S MAGNETOSHEATH: LOW PLASMA β CONDITIONS

B. Remya[1], B. T. Tsurutani[2], R. V. Reddy[1], G. S. Lakhina[1], B. J. Falkowski[2], E. Echer[3], and K.-H. Glassmeier[4]
[1] Indian Institute of Geomagnetism, Kalamboli Highway, New Panvel, Navi Mumbai, Maharashtra, India; remyaphysics@gmail.com
[2] Jet Propulsion Laboratory, California Institute of Technology, 4800 Oak Grove Drive, Pasadena, CA 91109, USA
[3] Instituto Nacional de Pesquisas Espaciais (INPE), Avenida Astronautas, 1758, P.O. Box 515, Sao Jose dos Campos, SP, Brazil
[4] Institute for Geophysics and Extraterrestrial Physics (IGEP), Mendelssohnstr.3, D-38106, Braunschweig, Germany
Received 2014 April 10; accepted 2014 July 16; published 2014 August 27

ABSTRACT

During 1999 August 18, both *Cassini* and *WIND* were in the Earth's magnetosheath and detected transverse electromagnetic waves instead of the more typical mirror-mode emissions. The *Cassini* wave amplitudes were as large as ∼14 nT (peak to peak) in a ∼55 nT ambient magnetic field B_0. A new method of analysis is applied to study these waves. The general wave characteristics found were as follows. They were left-hand polarized and had frequencies in the spacecraft frame ($f_{\rm scf}$) below the proton cyclotron frequency (f_p). Waves that were either right-hand polarized or had $f_{\rm scf} > f_p$ are shown to be consistent with Doppler-shifted left-hand waves with frequencies in the plasma frame $f_{pf} < f_p$. Thus, almost all waves studied are consistent with their being electromagnetic proton cyclotron waves. Most of the waves (∼55%) were found to be propagating along B_0 ($\theta_{kB_0} < 30^\circ$), as expected from theory. However, a significant fraction of the waves were found to be propagating oblique to B_0. These waves were also circularly polarized. This feature and the compressive ($[B_{\rm max} - B_{\rm min}]/B_{\rm max}$, where $B_{\rm max}$ and $B_{\rm min}$ are the maximum and minimum field magnitudes) nature (ranging from 0.27 to 1.0) of the waves are noted but not well understood at this time. The proton cyclotron waves were shown to be quasi-coherent, theoretically allowing for rapid pitch-angle transport of resonant protons. Because *Cassini* traversed the entire subsolar magnetosheath and *WIND* was in the dusk-side flank of the magnetosheath, it is surmised that the entire region was filled with these waves. In agreement with past theory, it was the exceptionally low plasma β (0.35) that led to the dominance of the proton cyclotron wave generation during this interval. A high-speed solar wind stream ($\langle V_{sw} \rangle = 598$ km s^{-1}) was the source of this low-β plasma.

Key words: instabilities – methods: data analysis – planets and satellites: individual (Earth, Cassini, WIND) – planets and satellites: magnetic fields – polarization

Online-only material: color figures

1. INTRODUCTION

On 1999 August 18, *Cassini–Huygens* flew past the Earth on its way to Saturn with a unique trajectory through the subsolar point of the Earth's magnetosheath. It crossed the Earth's foreshock, magnetosheath, and magnetosphere and then exited down the northern lobe of the magnetotail (at ∼1047 UT) after ∼10 hr of flight in the Earth's magnetosphere. Because the flyby was along the Sun–Earth line, it gave an ample opportunity to study the low-frequency electromagnetic plasma waves in the near-Earth environment. The opportunity has been well exploited, and the observations of low-frequency waves have been reported for the Earth's foreshock (Tsurutani et al. 2001, 2002a), magnetosheath (Southwood et al. 2001; Tsurutani et al. 2002a; Ogasawara et al. 2011), and magnetotail (Bogdanov et al. 2003). A detailed analysis of the *Cassini* magnetic-field observations in a general context is also reported in Khan et al. (2001); Southwood et al. (2001); and Tsurutani et al. (2002a).

Another spacecraft, *WIND*, was also in the Earth's magnetosheath on the same day, farther away from the Sun–Earth line, toward the dusk-side magnetosheath (−4.6, +23.3, +2.5 R_E (in Geocentric Solar Ecliptic; GSE at 0000 UT). The upstream solar wind conditions monitored by the Geotail (Figure 1) and *ACE* spacecraft indicate very low solar wind densities, which suggest that the Earth's magnetosheath was populated by a shocked high-speed solar wind stream (Tsurutani et al. 2002a). Tsurutani et al. (2002a) analyzed the *Cassini* magnetic field measurements and showed an abundance of low-frequency electromagnetic ion cyclotron waves with the highest amplitude reported up to that time in the Earth's magnetosheath. Motivated by their work, our paper explores the low-frequency waves in the magnetosheath from two satellites: *WIND* and *Cassini*, on the day of the CassiniEarth traversal. While *Cassini* was at the subsolar magnetosheath from ∼01:52 UT to ∼02:26 UT on 1999 August 18, *WIND* was at the dusk-flank magnetosheath during the same interval of time until it entered the magnetosphere at ∼03:20 UT. We will explore the detailed properties of this unusual event. We will analyze these magnetosheath waves using a new technique/program.

The Earth's magnetosheath region is reported to show frequent mirror-mode occurrences that are large-amplitude, nonoscillatory, quasi-periodic magnetic field magnitude structures. There are very few or no angular changes across the mirror-mode magnetic field structures, and the total (magnetic+plasma) pressure remains constant throughout. These are well studied theoretically (Chandrasekhar et al. 1958; Vedenov & Sagdeev 1958; Hasegawa 1969, 1975; Price et al. 1986; Pokhotelov et al. 2008; Hasegawa & Tsurutani 2011) and from an observational point of view (Tsurutani et al. 1982; Treumann et al. 1990, 2000; Lacombe et al. 1992; Anderson & Fuselier 1993; Chisham et al. 1998, 1999; Lucek et al. 1999a, 1999b, 2001; Dunlop et al. 2002; Tátrallyay & Erdös 2002, 2005; Constantinescu et al. 2003, 2006; Horbury et al. 2004; Narita & Glassmeier 2005; Narita et al. 2006; Soucek et al. 2008;

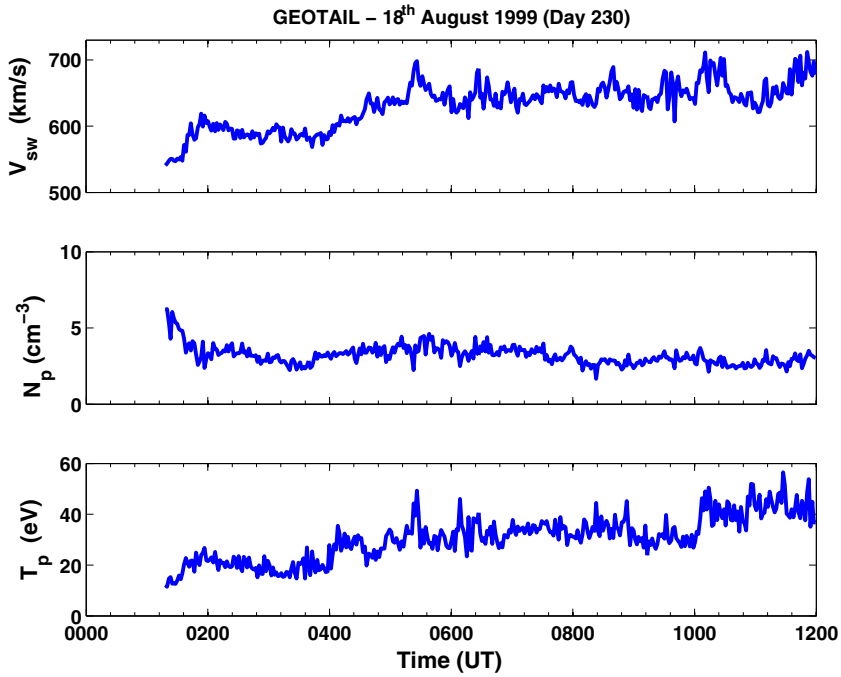

Figure 1. Upstream solar wind monitored by Geotail during the time of the *Cassini* Earth encounter.
(A color version of this figure is available in the online journal.)

Horbury & Lucek 2009; Tsurutani et al. 2011b). These structures arise due to an ion temperature anisotropy with $T_{\perp i} > T_{\|i}$, a condition that also excites the ion cyclotron instability (Kennel & Petschek 1966; Sckopke et al. 1990; Lacombe et al. 1992; Anderson & Fuselier 1993; Tsurutani et al. 2002a, 2002b). Theoretical studies on the competition between these two modes suggest that ion cyclotron modes have a higher linear growth rate in comparison to that of mirror modes in electron–proton plasmas (Price et al. 1986; Gary 1992; Gary et al. 1993; Remya et al. 2013). The chances of occurrence of mirror modes in high-beta plasmas are enhanced due to the presence of heavy ions like He^{2+} and O^{6+} (Price et al. 1986; Gary 1992; Remya et al. 2013), whereas the presence of anisotropic electrons favors the mirror-mode dominance over the ion cyclotron mode in low-beta plasmas as well (Remya et al. 2013). Simulation studies by Shoji et al. (2009, 2012) show that the large volume of oblique mirror waves in three-dimensional space consumes most of the free energy of the temperature anisotropy and thus hinders the growth of the ion cyclotron waves.

In the present paper, we examine the magnetic field data from the *WIND* and *Cassini* satellites to investigate the low-frequency magnetic field fluctuations in the Earth's magnetosheath region. We examine the plasma wave properties and characterize them statistically for the aforementioned intervals. The standard technique of minimum variance analysis (MVA) was originally used for the study of small-amplitude plasma waves in a comparatively steady magnetic field or plasma background (Smith & Tsurutani 1976). This technique can result in errors if used to determine high-amplitude wave properties. Hence a new technique/program called the Rosetta automatic wave analysis (RAWA) has been developed based on the technique initiated by Tsurutani et al. (2013) and has been applied to analyze the wave cycles in the present paper. The frequency, ellipticity, polarization, and angle of propagation of each wave cycle is determined and is characterized statistically to determine the wave properties for this event.

The method outlined and used here is also applicable to other situations where low-frequency waves need to be analyzed and characterized. The comet–solar wind interaction region with a plethora of pickup iongenerated low-frequency waves (Tsurutani et al. 1986a, 1986b, 1997, 2013; Glassmeier et al. 1987; Glassmeier & Neubauer 1993) is an ideal region to study such low-frequency waves. In-depth analyses of such waves in the interaction region of the solar wind and comet 67P/Churyumov–Gerasimenko during the Rosetta mission (Glassmeier et al. 2007) will provide the first indications of cometary pickup ions. The analysis tool presented here has been applied to Deep Space 1 (DS1) observations during the flyby of the Borrelly comet and will support the search for the pickup ions during the Rosetta mission cometary encounter.

2. DATA ANALYSIS METHODOLOGY

Figure 2 displays the trajectories of the *Cassini* and *WIND* spacecraft during the *Cassini* near-Earth flyby. The trajectories are in Geocentric Solar Magnetospheric (GSM) coordinates in the $X-Y$ (top panel) and $X-Z$ (bottom panel) planes. Hours in UT are marked along the trajectory. Model bow shock and magnetopause locations are also marked in the background. We study the time interval 01:52 UT to 02:26 UT, 1999 August 18, during which *Cassini* and *WIND* were in the Earth's magnetosheath. It is noted that *Cassini* entered the nose of the Earth's magnetosheath and went nearly along the Sun–Earth line. This point will be brought up later in the paper.

As mentioned previously, we use a new program called RAWA to analyze the plasma waves in the present paper. The raw magnetic field vectors are first low-pass filtered at values derived empirically for both *Cassini* and *WIND* magnetic field data. The low-pass values are the background magnetic field, and the high-pass filtered data are the wave fields. Wave cycles are selected from the high-pass filtered data and MVA are performed on individual wave cycles. An MVA consists

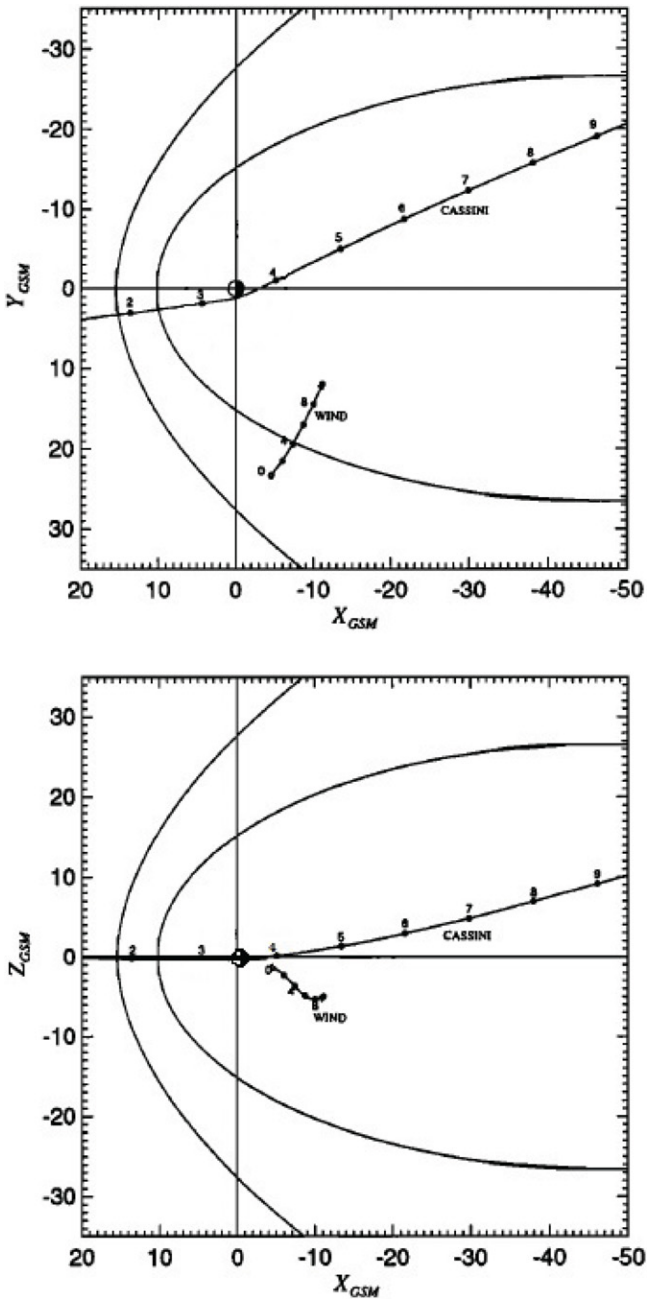

Figure 2. *Cassini* and *WIND* trajectories in GSM coordinates on 1999 August 18, during the *Cassini* Earth encounter. $X-Y$ (top panel) and $X-Z$ (bottom panel) cross sections are projected (taken from Khan et al. 2001 Figure 1).

of constructing the covariance matrix of the three magnetic field components, diagonalizing it, and then calculating its eigenvalues. These are called λ_1, λ_2, and λ_3. These correspond to maximum, intermediate, and minimum variance directions of the field components, respectively. Corresponding eigenvectors are calculated, and the magnetic field is then rotated into the minimum variance coordinates $\boldsymbol{B}_1$, $\boldsymbol{B}_2$, and $\boldsymbol{B}_3$, which form a right-handed coordinate system, where $\boldsymbol{B}_1 \times \boldsymbol{B}_2 = \boldsymbol{B}_3$. The $\boldsymbol{B}_3$ vector points along the direction of minimum variance and is also the direction of the wave vector $\boldsymbol{k}$ (Verkhoglyadova et al. 2010). The same technique was applied for the *WIND* magnetic field data.

The wave period (inverse frequency) is calculated directly using the duration of each wave cycle. The angle between the propagation vector $\boldsymbol{k}$ (direction of λ_3) and the ambient magnetic field direction is defined as the propagation angle θ_{kB_0}. The low-pass filtered data are used to calculate the ambient magnetic field direction for each individual wave cycle. The MVA method leaves a 180° uncertainty in determining the absolute direction of propagation (for single-spacecraft measurements and only using the three magnetic components; Sonnerup & Cahill 1967; Smith & Tsurutani 1976), and hence the values $\theta_{kB_0} > 90°$ are replaced by their corresponding complementary angles $(180° - \theta_{kB_0})$ so that one can visualize the range of values of θ_{kB_0}. Wave amplitudes are calculated as $(B_{\max} - B_{\min})$, where $B_{\max}$ and $B_{\min}$ are the maximum and minimum field magnitudes, and wave compression is calculated using the formula $(B_{\max} - B_{\min})/B_{\max}$.

The sense of rotation of the wave cycles is determined from hodograms where the magnetic field transverse components B_1 versus B_2 are plotted. The hodogram format can be used to determine whether the wave is left-hand (LH) or right-hand (RH) polarized. In our automated program, the ambient magnetic field is always plotted in the direction out of the page. The handedness of the rotation from the beginning to the end of the wave interval about the ambient magnetic field is used to indicate whether the wave is LH or RH polarized. The wave is linearly, circularly, or elliptically polarized depending on the value of ellipticity, which is defined by the ratio λ_1/λ_2. Ideally, $\lambda_1/\lambda_2 = 1$ indicates a circular wave, $\lambda_1/\lambda_2 > 1$ indicates an elliptical wave, and if $\lambda_1/\lambda_2 \gg 1$, the wave is linearly polarized (we found no such linearly polarized waves in this study). The ratio λ_1/λ_2 has uncertainties because we cannot get exactly 360° of phase rotation in an individual wave cycle due to data digitization and other factors. Therefore, the ratio will never be exactly 1.0 even if the wave is perfectly circularly polarized. The best way to determine the general ellipticity of a wave is by visual examination. The waves may be exactly circularly polarized even with ellipticity values $\lambda_1/\lambda_2 > 1$ (refer to Tables 1 and 2).

The frequencies and polarizations measured using the above technique are in the spacecraft (s/c) reference system. To obtain the intrinsic nature of a wave, one in the plasma frame of reference, we need to determine either the absolute wave propagation direction or the magnetosheath Doppler shift of the waves. As mentioned earlier, the MVA leaves a 180° ambiguity in determining the absolute direction of propagation. Simultaneous wave electric field measurements are needed to resolve this ambiguity. However, unfortunately, such electric field data were not available. We employ an alternate technique used by Tsurutani et al. (2013) and examine the waves that propagate orthogonally or nearly orthogonally to the solar wind direction, independent of its direction relative to B_0. These waves are not Doppler shifted in frequency or polarization and hence are observed in their plasma-frame state. We thus identify and reanalyze the events with $\theta_{kV_{sw}} > 70°$ with minimum Doppler shift. Here $\theta_{kV_{sw}}$ is the angle between the propagation vector $\boldsymbol{k}$ and solar wind velocity direction V_{sw}.

An attempt is made to quantitatively examine the coherence level of the waves. A significantly long wave packet (group of wave cycles) is selected from the wave data, and the MVA technique is applied for the wave interval. The magnetic field components B_1 and B_2 in the minimum variance coordinates are then subjected to cross-correlation analysis. The correlation coefficient at a variety of positive and negative lags will indicate the level of coherence of the waves. For a highly coherent wave, the cross-correlation coefficient at ~zero (one-fourth wavelength) lag will be 1.0, and the values at ±1 lag will be $\geqslant$0.95. This was shown to be the case for a whistler-mode wave known as the

Table 1
Magnetosheath Waves: *Cassini*, 1999 August 18 (0152–0226 UT)

Cycle	Start time (UT)	End time (UT)	λ_1/λ_2	λ_2/λ_3	θ_{kB_0} (deg)	$\theta_{kV_{sw}}$ (deg)	Pol.[a] (s/c)	T (sec)	Amp. (nT)	Comp.
1	0152:01.5	0152:03.8	2.5	8.3	86	10	LH	2.3	7.6	0.67
2	0152:07.8	0152:11.4	1.5	7.5	51	56	LH	3.5	13.6	0.65
3	0152:12.0	0152:15.0	4.3	4.6	63	30	LH	3.0	14.3	0.67
4	0152:17.1	0152:21.8	3.0	4.7	14	89	LH	4.6	5.4	0.55
5	0152:31.7	0152:34.6	2.2	6.6	55	46	LH	2.9	8.8	0.85
6	0152:35.5	0152:37.2	2.4	8.9	63	31	LH	1.6	3.5	0.52
7	0152:40.7	0152:43.4	2.1	7.6	53	44	RH	2.6	3.3	0.56
8	0152:47.3	0152:52.4	1.9	3.2	35	60	RHE	5.1	4.6	0.89
9	0152:53.3	0152:56.9	4.3	5.1	19	87	LH	3.5	5.0	0.75
10	0152:55.2	0152:59.2	3.2	33.4	50	38	LH	4.0	5.4	0.80
11	0153:11.0	0153:16.0	1.5	34.1	53	37	RH	4.9	6.7	0.84
12	0153:23.6	0153:29.0	1.8	4.6	64	36	RHE	5.4	9.8	0.72
13	0153:29.1	0153:33.9	1.8	6.1	25	79	LH	4.7	8.1	0.50
14	0153:37.3	0153:39.7	3.6	3.7	33	73	LH	2.4	4.8	0.73
15	0153:43.1	0153:46.9	2.6	19.4	83	11	LH	3.7	7.5	0.78
16	0153:45.9	0153:49.6	1.8	6.8	54	62	LH	3.6	6.9	0.77
17	0153:49.4	0153:50.9	2.1	8.3	84	5	RH	1.4	5.2	0.56
18	0153:54.4	0153:57.5	2.6	7.1	60	49	RH	3.1	8.1	0.71
19	0153:59.9	0154:03.8	2.9	7.5	15	72	LH	3.8	3.5	0.56
20	0154:05.7	0154:09.0	2.3	3.0	8	85	LH	3.2	5.3	0.82
21	0154:11.2	0154:13.8	3.2	7.7	53	49	LH	2.5	3.5	0.63
22	0154:16.9	0154:19.0	1.8	16.8	68	25	LH	2.0	4.0	0.80
23	0154:30.1	0154:35.0	1.9	8.7	9	84	LH	4.9	3.4	0.71
24	0154:49.3	0154:54.8	2.1	12.7	13	74	LH	5.5	5.3	0.66
25	0154:55.5	0155:01.7	1.8	5.0	42	85	LH	6.2	7.3	0.77
26	0155:02.7	0155:10.0	2.4	21.3	7	84	LH	7.3	4.5	0.80
27	0155:19.4	0155:22.4	6.6	17.2	39	47	RH	2.9	2.2	0.82
28	0155:22.8	0155:29.4	2.1	26.0	23	89	LH	6.5	7.6	0.75
29	0155:30.0	0155:36.5	4.3	5.0	19	80	LH	6.4	5.1	0.73
30	0155:44.6	0155:49.4	2.8	6.7	37	52	RH	4.8	4.9	0.98
31	0155:51.2	0155:55.6	2.3	6.1	23	69	LHE	4.3	3.8	0.59
32	0155:56.3	0156:03.7	2.2	11.1	11	79	LH	7.4	5.3	0.71
33	0156:04.8	0156:07.9	2.1	11.1	49	37	RH	3.0	4.1	0.71
34	0156:07.8	0156:14.1	1.4	10.0	4	88	LH	6.2	3.4	0.62
35	0156:16.5	0156:22.7	2.6	9.4	19	87	LH	6.2	4.6	0.80
36	0156:30.1	0156:33.9	1.7	39.1	28	71	LH	3.7	3.8	0.81
37	0156:43.4	0156:48.1	1.1	10.3	3	87	LH	4.6	3.6	0.44
38	0156:48.2	0156:53.2	1.6	73.3	14	71	LH	5.0	3.0	0.51
39	0156:56.7	0156:58.1	1.2	41.4	64	87	LH	1.4	1.6	0.56
40	0157:00.6	0157:04.2	1.7	5.7	7	88	LH	3.6	1.7	0.64
41	0157:05.7	0157:11.0	2.5	6.9	25	77	LH	5.2	4.7	0.43
42	0157:10.7	0157:16.2	4.7	13.7	21	72	LH	5.5	3.5	0.68
43	0157:14.2	0157:18.7	2.4	7.9	39	80	LH	4.4	3.7	0.96
44	0157:22.4	0157:29.5	3.4	6.2	9	79	LH	7.3	2.9	0.95
45	0157:39.3	0157:46.8	1.1	10.5	25	80	LH	7.5	5.7	0.63
46	0157:49.5	0157:52.1	3.1	11.8	75	31	LH	2.6	2.7	0.69
47	0158:00.7	0158:06.9	2.0	25.7	21	80	LH	6.2	4.6	0.72
48	0158:07.1	0158:12.0	1.6	7.2	14	80	LH	4.9	4.0	0.44
49	0158:13.7	0158:20.7	7.3	6.6	47	48	RH	7.0	6.0	0.79
50	0158:23.3	0158:27.4	1.9	9.8	53	42	LH	4.0	3.0	0.81
51	0158:28.1	0158:31.3	5.4	3.0	57	31	RHE	3.2	3.3	0.61
52	0158:31.9	0158:36.9	1.6	19.6	10	84	LH	4.9	2.9	0.72
53	0158:42.0	0158:50.8	3.8	12.6	2	82	LH	8.8	2.3	0.69
54	0158:53.3	0158:56.4	2.1	25.9	58	38	LH	3.0	2.7	0.94
55	0158:57.9	0158:59.5	4.3	21.0	65	19	LH	1.6	1.4	0.39
56	0159:08.9	0159:14.2	2.6	28.0	17	68	LH	5.3	3.6	0.84
57	0159:14.0	0159:20.0	1.1	51.8	13	81	LH	6.0	2.4	0.40
58	0159:20.4	0159:26.5	1.4	11.1	18	81	LH	6.1	4.6	0.67
59	0159:37.6	0159:39.9	1.9	3.1	71	84	LH	2.3	2.5	0.43
60	0159:40.6	0159:44.9	8.5	8.7	4	82	RHE	4.2	1.5	0.85
61	0159:54.6	0159:56.1	7.1	49.4	84	14	LH	1.5	1.5	0.69
62	0200:03.6	0200:09.1	2.5	19.7	27	81	LH	5.5	3.9	0.59
63	0200:09.1	0200:13.5	1.4	50.5	18	66	LH	4.4	3.0	0.62
64	0200:17.3	0200:24.3	2.5	27.7	14	83	LH	7.0	2.8	0.71
65	0200:22.7	0200:27.4	3.7	5.5	11	87	LH	4.6	1.7	0.77

Table 1
(Continued)

Cycle	Start time (UT)	End time (UT)	λ_1/λ_2	λ_2/λ_3	θ_{kB_0} (deg)	$\theta_{kV_{sw}}$ (deg)	Pol.[a] (s/c)	T (sec)	Amp. (nT)	Comp.
66	0200:26.7	0200:32.5	3.3	7.1	42	51	LH	5.8	5.9	0.87
67	0200:35.4	0200:38.3	6.7	5.2	77	42	LH	2.8	3.1	0.79
68	0200:45.0	0200:49.9	4.6	8.1	16	68	RH	4.8	4.7	0.57
69	0201:05.5	0201:13.0	4.0	5.6	11	82	LH	7.5	4.9	0.76
70	0201:22.5	0201:28.1	4.2	13.1	4	80	LH	5.5	2.2	0.72
71	0201:31.7	0201:36.4	1.6	102.9	74	17	RH	4.7	4.5	0.75
72	0201:36.8	0201:41.2	3.6	6.1	23	65	LH	4.4	2.0	0.72
73	0201:41.3	0201:47.0	3.8	9.0	14	88	RH	5.6	3.0	0.72
74	0201:45.7	0201:50.2	5.2	4.8	58	50	LH	4.5	3.2	0.65
75	0201:57.4	0202:03.2	5.8	19.5	6	77	RH	5.8	1.9	0.83
76	0202:03.0	0202:06.0	3.4	15.6	45	68	LH	3.0	2.9	0.79
77	0202:10.0	0202:14.8	1.2	38.7	7	83	LH	4.7	2.6	0.52
78	0202:14.9	0202:22.1	1.4	34.9	14	89	LH	7.2	4.4	0.58
79	0202:28.8	0202:37.3	1.3	13.8	12	77	LH	8.5	2.8	0.42
80	0202:34.8	0202:40.0	3.0	8.8	34	52	RH	5.2	4.0	0.68
81	0202:42.4	0202:49.1	3.0	195.6	6	88	LH	6.7	1.7	0.45
82	0202:46.1	0202:51.8	2.0	157.6	9	88	LH	5.7	1.5	0.86
83	0202:51.4	0202:55.5	2.5	6.8	26	85	LH	4.1	2.4	0.79
84	0202:55.0	0203:00.2	9.8	5.0	17	76	RH	5.2	3.2	0.85
85	0203:01.9	0203:08.0	4.7	8.8	5	85	LH	6.0	2.2	0.67
86	0203:08.2	0203:10.3	1.1	6.2	64	44	LH	2.1	2.7	0.87
87	0203:17.4	0203:24.4	2.7	28.9	16	70	LH	6.9	2.1	0.96
88	0203:23.4	0203:26.3	2.2	3.3	25	80	LH	3.0	1.9	0.87
89	0203:34.7	0203:42.4	13.8	4.6	27	69	RHE	7.6	2.9	0.93
90	0203:40.9	0203:50.9	8.4	3.3	5	87	LHE	9.9	4.1	0.76
91	0203:57.9	0204:03.0	2.5	7.1	12	79	LH	5.0	4.8	0.84
92	0204:03.4	0204:07.0	1.5	7.4	29	66	RH	3.5	3.0	0.77
93	0204:09.9	0204:15.8	4.6	19.3	16	71	LHE	5.9	2.3	0.84
94	0204:12.7	0204:17.1	3.8	69.1	11	73	LH	4.4	1.4	0.82
95	0204:15.6	0204:20.6	6.9	10.4	19	86	LH	4.9	2.2	0.71
96	0204:25.6	0204:32.0	3.2	28.2	10	73	LH	6.3	2.3	0.71
97	0204:31.8	0204:37.0	3.2	13.4	21	62	LH	5.2	3.0	0.81
98	0204:41.6	0204:47.6	3.6	25.0	44	53	RH	6.0	4.4	0.72
99	0204:45.2	0204:49.6	3.9	11.7	55	48	LH	4.3	3.1	0.38
100	0204:53.5	0204:58.1	6.9	3.9	10	73	RHE	4.6	1.4	0.89
101	0205:01.6	0205:06.7	1.9	4.9	34	50	LHE	5.1	3.6	0.85
102	0205:09.7	0205:15.5	3.7	6.7	46	57	LH	5.7	5.2	0.87
103	0205:13.0	0205:18.8	3.0	3.1	33	58	LH	5.7	3.5	0.87
104	0205:18.5	0205:23.9	2.6	10.8	43	63	LH	5.4	3.4	0.85
105	0205:23.5	0205:27.8	5.7	54.2	12	83	LH	4.2	0.5	0.64
106	0205:31.1	0205:35.1	2.0	31.7	8	88	LH	4.0	1.3	0.38
107	0205:33.3	0205:39.2	1.6	14.0	24	81	LH	5.9	3.3	0.60
108	0205:38.2	0205:43.8	2.7	8.0	69	72	LH	5.5	4.1	0.50
109	0205:44.1	0205:50.4	4.4	26.9	10	85	RH	6.3	2.3	0.53
110	0205:59.4	0206:04.9	3.0	11.0	20	87	LH	5.4	2.5	0.47
111	0206:04.5	0206:11.0	5.0	15.1	21	64	LH	6.5	3.1	0.79
112	0206:13.8	0206:20.4	1.4	27.7	27	69	LH	6.6	3.4	0.66
113	0206:21.9	0206:30.8	1.0	34.0	86	15	LH	8.8	3.8	0.59
114	0206:33.7	0206:40.3	2.0	19.4	22	75	LH	6.6	4.9	0.58
115	0206:40.7	0206:47.2	1.7	5.8	7	81	LH	6.4	1.9	0.71
116	0206:45.0	0206:51.2	1.7	30.0	17	77	LH	6.1	2.3	0.52
117	0206:59.5	0207:03.5	9.0	3.6	80	57	LH	4.0	3.0	0.65
118	0207:11.5	0207:17.4	1.4	12.2	10	87	LH	5.9	4.5	0.55
119	0207:13.1	0207:18.3	1.3	65.6	5	88	LH	5.1	2.4	0.68
120	0207:17.9	0207:22.0	6.4	8.4	51	32	RH	4.0	4.6	0.75
121	0207:21.7	0207:29.2	4.7	41.0	70	31	LH	7.5	6.2	0.69
122	0207:35.6	0207:42.0	1.9	12.8	34	52	RH	6.3	5.1	0.53
123	0207:50.3	0207:52.9	1.7	17.5	71	23	LH	2.6	3.4	0.61
124	0207:54.3	0208:01.5	1.2	28.6	27	69	LH	7.1	2.9	0.74
125	0208:05.8	0208:13.3	1.2	37.9	12	86	LH	7.5	2.0	0.52
126	0208:18.7	0208:27.6	3.5	3.1	86	56	LH	8.8	6.2	0.80
127	0208:26.2	0208:29.9	8.2	3.4	63	35	LH	3.7	5.1	0.76
128	0208:27.8	0208:34.2	4.9	12.7	21	74	RH	6.4	2.9	0.76
129	0208:30.0	0208:37.2	2.1	9.0	33	63	LH	7.1	6.5	0.61
130	0208:33.8	0208:38.7	1.2	146.7	39	61	LH	4.8	5.1	0.67

Table 1
(Continued)

Cycle	Start time (UT)	End time (UT)	λ_1/λ_2	λ_2/λ_3	θ_{kB_0} (deg)	$\theta_{kV_{sw}}$ (deg)	Pol.[a] (s/c)	T (sec)	Amp. (nT)	Comp.
131	0208:59.4	0209:06.7	3.6	8.5	54	58	LH	7.2	7.1	0.50
132	0209:07.1	0209:12.6	6.4	9.6	68	28	LH	5.5	3.5	0.74
133	0209:09.5	0209:13.2	2.9	39.9	79	18	LH	3.6	3.5	0.70
134	0209:16.8	0209:24.2	2.5	14.9	66	18	LHE	7.4	6.8	0.72
135	0209:23.2	0209:26.7	7.6	19.5	74	33	RH	3.5	2.7	0.80
136	0209:30.9	0209:37.7	3.1	20.6	31	65	LHE	6.7	3.8	0.77
137	0209:45.7	0209:48.6	5.7	12.8	40	44	LH	2.9	1.6	0.35
138	0209:54.1	0209:56.9	9.4	3.4	17	77	LH	2.7	2.5	0.76
139	0209:56.2	0210:01.2	1.9	18.0	34	52	LH	5.3	4.2	0.79
140	0210:14.5	0210:18.6	1.2	8.6	62	36	LH	4.0	3.5	0.62
141	0210:24.1	0210:29.9	2.4	6.5	35	77	LH	5.7	6.3	0.64
142	0210:28.2	0210:33.4	8.7	7.0	41	40	LH	5.2	4.1	0.72
143	0211:02.0	0211:08.4	1.0	12.4	42	40	LH	6.4	6.0	0.62
144	0211:14.0	0211:20.6	4.8	5.7	2	81	LH	6.5	3.3	0.80
145	0211:26.6	0211:29.9	4.9	3.9	33	86	LH	3.3	2.6	0.54
146	0211:29.7	0211:34.9	5.7	7.3	40	56	RH	5.2	5.3	0.72
147	0211:36.8	0211:43.8	2.7	3.1	35	62	LH	6.9	6.6	0.80
148	0211:43.6	0211:54.3	1.3	6.5	42	51	LH	10.7	5.8	0.72
149	0211:53.1	0212:01.0	4.8	4.8	18	78	LH	7.9	4.5	0.70
150	0212:20.2	0212:24.9	6.6	3.9	48	45	LH	4.6	2.6	0.77
151	0212:29.6	0212:35.0	2.6	3.6	13	79	LH	5.4	5.1	0.68
152	0212:33.3	0212:37.1	5.5	6.1	78	46	LH	3.8	2.8	0.67
153	0212:38.3	0212:47.7	1.9	11.3	31	65	LH	9.3	5.5	0.58
154	0212:59.6	0213:06.0	2.4	14.0	87	73	LH	6.3	6.4	0.67
155	0213:12.3	0213:16.6	1.8	8.8	42	42	LH	4.2	3.4	0.82
156	0213:17.1	0213:20.0	1.8	18.0	29	89	RH	2.9	1.8	0.34
157	0213:20.0	0213:27.3	2.3	7.4	5	84	RH	7.2	2.2	0.80
158	0213:36.5	0213:42.7	2.4	3.1	74	71	RH	6.1	4.1	0.92
159	0214:07.3	0214:12.6	4.0	23.5	14	89	LH	5.2	1.5	0.44
160	0214:29.4	0214:32.5	4.2	31.4	33	72	LH	3.0	1.9	0.79
161	0214:55.4	0215:01.6	6.2	14.4	10	72	RH	6.1	1.1	0.52
162	0215:03.6	0215:06.1	5.1	14.2	39	58	RH	2.5	1.5	0.67
163	0215:06.2	0215:12.0	4.9	4.0	30	73	LH	5.8	3.6	0.69
164	0215:31.3	0215:34.0	4.8	8.8	4	77	LH	2.6	1.8	0.63
165	0215:34.6	0215:36.4	13.1	17.8	73	24	LHE	1.8	1.3	0.88
166	0215:39.8	0215:42.2	3.6	4.7	71	14	LH	2.3	2.1	0.43
167	0215:49.1	0215:52.2	4.8	4.1	20	77	RH	3.0	2.9	0.75
168	0215:53.2	0215:56.3	10.5	23.6	18	73	RHE	3.0	1.0	0.56
169	0216:02.7	0216:09.0	3.2	9.5	33	66	LH	6.3	4.4	0.71
170	0216:09.2	0216:17.1	11.3	4.6	36	46	RHE	7.9	7.2	0.84
171	0216:29.1	0216:37.4	15.4	8.3	74	7	LH	8.3	4.5	0.97
172	0216:47.7	0216:58.2	1.6	3.8	57	40	RH	10.5	7.2	0.57
173	0216:56.8	0216:59.3	7.5	159.1	6	78	RH	2.4	0.5	0.27
174	0217:03.3	0217:06.8	6.7	3.1	57	25	LHE	3.4	1.7	0.61
175	0217:08.7	0217:11.5	4.0	8.7	21	61	LH	2.8	1.3	0.67
176	0217:20.3	0217:26.6	4.9	20.6	15	81	LH	6.2	2.7	0.70
177	0217:30.6	0217:33.8	3.7	6.0	78	39	RHE	3.1	2.4	0.78
178	0217:44.3	0217:46.2	5.4	4.9	61	43	LH	1.8	2.1	0.80
179	0217:55.0	0218:01.3	6.0	9.8	41	55	RH	6.3	2.5	0.72
180	0218:15.7	0218:19.8	2.9	33.8	10	72	LH	4.1	1.4	0.94
181	0218:22.0	0218:25.1	8.4	7.0	15	79	LH	3.1	1.2	0.87
182	0218:25.0	0218:32.5	5.5	17.2	72	26	LH	7.5	6.7	0.91
183	0218:31.9	0218:36.5	1.9	18.4	28	54	LH	4.6	4.0	0.70
184	0218:38.1	0218:42.8	3.5	4.7	50	49	RH	4.7	2.8	0.65
185	0218:50.5	0218:52.8	2.6	32.4	15	81	RHE	2.2	0.7	0.31
186	0218:53.6	0218:58.3	2.3	17.7	26	57	LH	4.6	2.4	0.65
187	0219:35.5	0219:38.4	6.9	3.5	24	65	LH	2.8	3.2	0.91
188	0219:46.3	0219:50.7	6.7	4.8	30	63	LH	4.3	3.1	0.82
189	0220:19.4	0220:22.4	5.1	60.2	13	70	LH	3.0	1.5	0.75
190	0220:22.5	0220:27.8	7.1	51.3	11	84	LH	5.2	2.6	0.79
191	0220:29.3	0220:33.4	21.1	3.7	15	70	LH	4.0	1.2	0.77
192	0220:48.3	0220:52.1	3.2	30.3	16	66	LH	3.8	1.6	0.78
193	0220:52.8	0220:56.5	1.1	43.0	20	82	LH	3.7	2.6	0.56
194	0221:00.2	0221:02.5	3.4	6.0	30	70	RHE	2.3	1.6	0.54
195	0221:02.5	0221:08.1	13.2	5.3	67	14	RH	5.5	3.0	0.90

Table 1
(Continued)

Cycle	Start time (UT)	End time (UT)	λ_1/λ_2	λ_2/λ_3	θ_{kB_0} (deg)	$\theta_{kV_{sw}}$ (deg)	Pol.[a] (s/c)	T (sec)	Amp. (nT)	Comp.
196	0221:24.9	0221:26.6	2.5	75.7	6	76	LH	1.6	0.8	0.77
197	0221:37.8	0221:41.0	4.3	13.6	29	52	LH	3.2	1.4	0.94
198	0221:41.3	0221:44.8	2.3	26.3	2	83	LH	3.5	1.3	0.60
199	0221:47.9	0221:51.1	3.1	14.9	17	81	LH	3.2	2.0	0.77
200	0221:54.4	0221:57.3	1.9	51.2	29	57	LH	2.8	2.1	0.62
201	0221:56.6	0221:59.3	6.9	12.5	53	46	LHE	2.6	2.7	0.77
202	0222:04.4	0222:07.9	3.8	8.0	24	67	LH	3.4	1.8	0.66
203	0222:15.7	0222:19.8	21.0	4.0	5	77	LH	4.0	1.7	0.92
204	0222:23.0	0222:26.4	6.2	4.8	11	75	LH	3.4	2.5	0.86
205	0222:35.6	0222:37.7	3.8	100.6	12	85	RH	2.1	0.6	0.85
206	0222:37.5	0222:40.5	3.9	17.3	25	85	LH	2.9	1.4	0.75
207	0222:41.8	0222:44.2	5.8	8.3	25	58	LH	2.3	2.0	0.80
208	0222:51.5	0222:57.1	8.6	6.0	19	66	RHE	5.6	2.8	0.87
209	0222:55.0	0222:58.1	2.1	7.2	28	75	LH	3.0	2.1	0.78
210	0223:04.1	0223:06.1	3.6	9.5	13	86	RH	2.0	1.2	0.91
211	0223:12.5	0223:18.0	11.9	7.6	6	77	RHE	5.5	1.6	0.84
212	0223:19.9	0223:21.1	4.0	26.6	42	64	LHE	1.2	1.1	0.54
213	0223:21.9	0223:23.2	9.6	74.9	11	71	RHE	1.3	0.7	0.80
214	0223:43.8	0223:44.9	5.4	11.7	30	66	LH	1.1	1.0	0.94
215	0223:45.4	0223:47.1	1.5	9.7	21	79	LH	1.7	1.4	0.49
216	0223:57.2	0224:00.0	4.7	19.3	20	79	LH	2.7	2.0	0.83
217	0224:00.6	0224:02.6	5.0	7.9	80	20	LH	1.9	1.7	0.59
218	0224:04.2	0224:06.9	1.2	82.9	8	80	LH	2.6	1.3	0.78
219	0224:11.0	0224:12.5	1.3	6.0	6	87	LH	1.5	1.0	0.68
220	0224:12.1	0224:13.4	2.3	4.5	30	80	LH	1.2	1.5	0.41
221	0224:13.8	0224:15.5	4.2	16.2	18	77	LH	1.7	1.4	0.87
222	0224:16.2	0224:19.2	2.1	8.2	9	86	LH	3.0	1.5	0.64
223	0224:20.4	0224:21.5	5.8	15.6	16	78	RH	1.1	1.1	0.70
224	0224:22.7	0224:24.3	3.5	16.2	32	62	LH	1.6	1.2	0.82
225	0224:25.2	0224:27.0	6.6	12.9	5	88	LH	1.7	1.1	0.65
226	0225:19.4	0225:21.8	5.4	3.7	78	21	LH	2.3	1.2	0.63
227	0225:38.7	0225:41.1	4.5	12.0	35	73	LH	2.4	2.6	0.53
228	0225:42.8	0225:45.6	3.8	15.3	43	47	LH	2.8	4.5	0.55
229	0225:50.3	0225:52.3	1.0	70.5	15	88	RH	2.0	2.9	0.63

Note. [a] LH/RH—Left/Right-hand circular, LHE/RHE—Left/Right-hand elliptical polarizations.

electromagnetic chorus in the Earth's magnetosphere (Tsurutani et al. 2011a). For lesser coherent waves, the peak correlation coefficient at zero lag can be significantly less than 1.0 (say 0.5) with further decrease in amplitude at larger lags. Waves with these characteristics have been called "quasi-coherent.Pure turbulence will have little or no correlation between the B_1 and B_2 components.

The level of wave coherence is highly important for the scattering of energetic particles. Particle cyclotron resonant interaction with a coherent wave leads to "pitch-angle transport," a large-pitch angle change from a single-wave packet–particle interaction (Tsurutani et al. 2009; Lakhina et al. 2010).

3. MAGNETOSHEATH WAVES

3.1. Observational Results from Cassini

The *Cassini* magnetometer provided magnetic field measurements at a rate of 32 vectors/second. This high data rate is used in our analysis. Figure 3 displays the magnetic field components observed by *Cassini* in the Earth's bow shock, magnetosheath, and magnetopause (0150–0230 UT) during its Earth flyby. The magnetic field is in GSM coordinates. The magnetic field magnitude increases from ~30 nT just downstream of the bow shock to ~60 nT close to the magnetopause. There are large transverse amplitude fluctuations throughout the magnetosheath. This can be seen in the magnetic field transverse components B_x and B_y. There are small magnetic magnitude fluctuations at 0206 UT. The low-pass background field and the remainder high-pass magnetic fluctuations are given in Figures 4 and 5, respectively. Figure 4 shows that the magnetosheath magnetic field is directed primarily orthogonal to the Sun–Earth line. Just downstream of the bow shock the magnetic field is $B_x = \sim -1$ nT, $B_y = \sim 14$ nT, and $B_z = \sim -24$ nT, and just prior to crossing the magnetopause, $B_x = \sim -7$ nT, $B_y = \sim 37$ nT, and $B_z = \sim -35$ nT. Figure 5 shows large-amplitude ~8 to ~10 nT fluctuations that were present throughout the entire magnetosheath. Various wave cycles were analyzed from this high-pass wave data. The MVA is applied individually to each wave interval.

3.1.1. Wave Events

Figure 6 gives the results of a minimum variance analysis performed on a number of individual wave cycles. The hodograms shown in the figure correspond to various locations in the magnetosheath. The two upper panels correspond to waves immediately downstream of the bow shock, the middle panels show wave events near the center of the magnetosheath, and the bottom panels indicate wave cycles close to the magnetopause. The ratio λ_1/λ_2, angle θ_{kB_0}, UT, and the sense of rotation or

Table 2
Magnetosheath Waves{:} *WIND*, 1999 August 18 (0152–0226 UT)

Cycle	Start time (UT)	End time (UT)	λ_1/λ_2	λ_2/λ_3	θ_{kB_0} (deg)	$\theta_{kV_{sw}}$ (deg)	Pol.[a] (s/c)	T (sec)	Amp. (nT)	Comp.
1	0152:04.6	0152:08.7	5.1	3.0	51	76	RHE	4.0	2.4	0.68
2	0152:33.0	0152:38.9	52.0	6.5	29	77	LHE	5.9	0.7	0.88
3	0152:38.7	0152:43.5	5.7	5.5	44	82	LH	4.8	0.8	0.69
4	0152:46.3	0152:50.5	2.6	6.2	70	31	LH	4.2	2.0	0.65
5	0152:50.8	0152:55.0	2.4	3.1	35	69	RH	4.2	1.3	0.79
6	0152:55.6	0153:02.9	4.6	6.0	27	40	RH	7.3	1.3	0.72
7	0153:13.4	0153:19.2	3.3	3.4	58	83	LH	5.8	0.7	0.68
8	0153:27.2	0153:32.5	2.8	6.1	62	54	RH	5.2	2.3	0.85
9	0153:48.1	0153:50.8	1.5	12.7	14	57	LH	2.6	0.4	0.86
10	0153:52.0	0153:55.2	7.0	7.4	82	58	LHE	3.2	1.9	0.74
11	0153:54.5	0153:59.2	2.9	16.5	31	27	RHE	4.7	1.4	0.77
12	0154:20.7	0154:23.9	15.8	4.0	27	34	RHE	3.2	0.7	0.73
13	0154:24.4	0154:27.8	2.2	6.4	53	29	LH	3.4	1.5	0.60
14	0154:35.8	0154:39.7	2.2	14.2	38	25	RH	3.9	2.0	0.84
15	0154:43.4	0154:47.1	1.5	6.6	52	83	RH	3.6	1.7	0.77
16	0154:49.2	0154:53.8	2.0	11.1	54	66	LH	4.6	1.3	0.71
17	0154:54.0	0154:58.9	3.7	13.0	24	60	LH	4.8	1.0	0.76
18	0155:09.8	0155:12.3	2.9	31.9	62	42	RH	2.4	1.9	0.78
19	0155:14.0	0155:16.4	6.0	8.1	34	54	LHE	2.3	0.7	0.71
20	0155:21.5	0155:26.7	1.8	5.2	87	76	LH	5.2	1.8	0.76
21	0155:31.4	0155:37.2	4.1	3.4	18	57	RH	5.8	1.5	0.78
22	0155:54.8	0156:00.3	2.3	16.0	89	70	LH	5.5	3.1	0.66
23	0156:14.9	0156:19.8	2.4	93.8	11	58	RH	4.9	0.9	0.80
24	0156:18.9	0156:23.6	8.0	6.5	89	78	LHE	4.6	3.7	0.86
25	0156:24.8	0156:30.0	2.2	2.1	18	76	LH	5.2	1.4	0.70
26	0156:34.5	0156:36.7	9.6	15.2	64	15	LH	2.1	0.8	0.44
27	0157:01.4	0157:02.8	1.9	12.4	21	85	LH	1.3	0.8	0.32
28	0157:09.3	0157:11.1	2.3	35.7	50	85	LH	1.7	0.6	0.75
29	0157:38.0	0157:41.2	1.2	20.6	3	75	LH	3.1	0.4	0.96
30	0157:43.1	0157:49.1	1.6	6.8	7	84	LH	5.9	0.7	0.91
31	0157:50.3	0157:55.0	4.8	5.3	43	80	LH	4.6	0.7	0.83
32	0158:12.2	0158:15.6	1.9	6.4	31	85	LH	3.3	0.5	0.81
33	0158:15.7	0158:23.0	4.1	52.1	11	81	LH	7.3	0.7	0.80
34	0158:26.6	0158:33.1	4.2	27.2	0	78	LH	6.5	0.4	0.79
35	0158:32.7	0158:39.7	2.4	7.4	10	72	LH	6.9	0.9	0.83
36	0158:46.7	0159:03.4	7.5	3.9	84	50	LH	16.6	2.5	0.85
37	0159:05.1	0159:08.5	1.6	11.6	9	81	LH	3.3	0.7	0.78
38	0159:08.3	0159:11.7	1.7	14.6	2	86	RH	3.4	0.4	0.75
39	0159:16.3	0159:18.4	2.6	7.0	75	22	RH	2.1	0.7	0.53
40	0200:19.8	0200:25.4	2.3	8.8	12	70	LH	5.6	0.9	0.78
41	0200:28.8	0200:31.1	8.0	6.2	88	75	LH	2.3	0.6	0.72
42	0200:32.2	0200:40.6	4.4	6.0	11	88	LH	8.3	0.7	0.92
43	0200:42.8	0200:49.1	3.0	107.3	9	70	RH	6.3	0.8	0.87
44	0201:29.6	0201:33.3	1.8	25.8	22	69	LH	3.6	0.5	0.76
45	0201:44.5	0201:50.2	5.8	6.8	16	78	LHE	5.7	1.1	0.87
46	0201:51.9	0201:56.7	2.2	25.4	7	79	LH	4.7	0.4	0.87
47	0202:06.7	0202:12.2	14.3	9.2	27	79	LHE	5.5	0.6	0.87
48	0202:11.3	0202:19.2	3.3	7.4	19	86	RHE	7.9	0.7	0.86
49	0202:19.2	0202:24.5	2.4	6.2	36	86	LH	5.3	1.4	0.85
50	0202:48.7	0202:50.9	1.5	23.5	11	72	LH	2.2	0.4	0.53
51	0202:51.7	0202:57.9	2.6	14.0	9	68	LH	6.2	0.7	0.70
52	0203:08.5	0203:14.2	5.5	30.2	9	80	LH	5.7	1.3	0.82
53	0203:20.7	0203:26.3	2.2	13.6	2	75	LH	5.6	0.7	0.75
54	0203:40.9	0203:45.4	2.5	7.6	13	85	LHE	4.5	0.9	0.90
55	0203:38.0	0203:44.0	5.8	11.9	10	83	LH	5.9	0.9	0.70
56	0203:44.9	0203:49.9	3.3	6.8	7	80	LH	4.9	0.7	0.87
57	0203:50.0	0203:53.4	4.3	4.1	61	67	LH	3.4	0.6	0.82
58	0203:59.0	0204:03.0	1.7	17.4	32	39	LH	4.0	0.7	0.71
59	0204:04.8	0204:11.6	3.1	11.3	25	62	LH	6.8	1.1	0.70
60	0204:17.0	0204:20.6	3.8	30.4	6	77	LH	3.5	0.4	0.82
61	0204:23.5	0204:29.9	2.1	24.2	7	79	LH	6.4	0.6	0.77
62	0204:28.0	0204:33.1	2.7	20.2	14	76	LH	5.1	0.6	0.76
63	0204:44.5	0204:51.1	4.6	7.9	7	82	LH	6.5	0.8	0.95
64	0204:54.8	0204:58.3	3.6	14.3	33	84	LH	3.5	0.8	0.66
65	0205:06.9	0205:12.5	6.7	14.2	13	83	RH	5.6	0.9	0.88

Table 2
(Continued)

Cycle	Start time (UT)	End time (UT)	λ_1/λ_2	λ_2/λ_3	θ_{kB_0} (deg)	$\theta_{kV_{sw}}$ (deg)	Pol.[a] (s/c)	T (sec)	Amp. (nT)	Comp.
66	0205:40.4	0205:46.2	1.4	38.9	3	77	LH	5.8	0.6	0.88
67	0205:36.6	0205:39.7	5.5	14.3	24	52	RH	3.1	0.5	0.67
68	0205:40.6	0205:47.5	1.9	39.9	2	75	LH	6.9	0.7	0.92
69	0205:57.2	0206:02.1	2.4	21.4	14	86	LH	4.8	1.0	0.83
70	0206:02.9	0206:06.7	1.6	28.9	24	64	LH	3.7	0.9	0.53
71	0206:05.4	0206:11.0	1.8	6.2	28	55	LH	5.6	1.7	0.71
72	0206:13.9	0206:18.0	2.3	16.6	7	66	LH	4.1	0.8	0.65
73	0206:39.5	0206:40.3	1.7	36.3	55	18	LH	0.7	1.0	0.32
74	0206:46.0	0206:51.1	3.5	28.3	14	82	LH	5.1	0.9	0.63
75	0206:58.3	0207:01.4	2.6	16.1	6	66	RHE	3.1	0.6	0.89
76	0207:02.6	0207:07.0	1.7	80.2	12	55	RH	4.3	1.3	0.73
77	0207:07.0	0207:11.6	1.9	20.3	9	57	RH	4.6	1.5	0.70
78	0207:11.6	0207:15.2	2.6	39.4	28	41	LH	3.6	2.2	0.68
79	0207:16.5	0207:21.5	1.9	38.6	9	58	LH	4.9	0.9	0.57
80	0207:17.2	0207:22.1	1.8	14.5	10	55	LH	4.9	1.0	0.57
81	0207:23.8	0207:28.9	1.6	23.9	4	70	LH	5.1	0.5	0.64
82	0207:32.0	0207:37.7	2.7	60.3	7	65	LH	5.7	0.6	0.70
83	0207:37.6	0207:43.9	2.5	29.0	5	60	LH	6.3	0.4	0.85
84	0207:43.8	0207:49.4	2.8	105.2	12	66	LH	5.6	0.6	0.57
85	0207:50.8	0207:57.0	4.8	30.8	10	55	LH	6.1	0.4	0.84
86	0207:57.5	0208:04.6	3.0	13.9	4	63	LH	7.1	0.8	0.97
87	0208:01.3	0208:06.6	1.6	218.5	14	51	LH	5.2	0.8	0.55
88	0208:26.3	0208:31.4	4.5	104.6	12	73	LH	5.1	0.5	0.62
89	0208:40.6	0208:44.4	3.8	4.4	13	78	LH	3.7	0.5	0.74
90	0209:08.0	0209:12.3	5.0	29.5	3	69	LHE	4.3	0.3	0.75
91	0209:32.7	0209:36.8	1.7	5.5	26	46	LHE	4.1	0.6	0.48
92	0209:38.1	0209:42.8	7.7	15.1	37	47	RHE	4.6	0.8	0.95
93	0209:42.9	0209:46.7	10.1	17.7	5	68	LHE	3.7	0.4	0.96
94	0209:46.0	0209:51.1	26.6	17.4	6	64	RHE	5.0	0.4	0.95
95	0209:51.0	0209:54.3	1.2	50.7	13	63	LH	3.3	0.2	0.45
96	0210:07.5	0210:09.4	2.1	12.8	13	67	LH	1.9	0.5	0.67
97	0210:10.0	0210:12.3	2.4	23.9	14	74	LH	2.3	0.5	0.68
98	0210:27.0	0210:30.6	1.7	14.8	14	75	LH	3.6	1.2	0.87
99	0210:36.1	0210:39.0	1.5	4.4	47	63	LH	2.9	0.9	0.45
100	0211:08.4	0211:12.8	4.1	18.0	4	67	LH	4.4	0.3	0.85
101	0211:13.9	0211:17.1	4.8	4.6	39	66	LH	3.2	0.3	0.97
102	0211:20.6	0211:26.8	6.1	3.6	59	65	LH	6.1	1.1	0.85
103	0211:24.4	0211:28.9	5.1	10.7	37	61	LH	4.5	0.8	0.86
104	0211:31.6	0211:35.4	3.0	8.1	39	75	LH	3.7	0.7	0.72
105	0211:35.7	0211:39.4	4.2	42.9	9	74	LH	3.6	0.2	0.80
106	0211:43.6	0211:48.5	4.6	6.4	12	58	LH	4.8	0.7	0.88
107	0212:53.4	0212:57.5	1.6	68.0	4	62	LH	4.0	0.5	0.88
108	0213:05.2	0213:10.2	1.9	27.8	8	69	LH	4.9	0.7	0.60
109	0213:10.5	0213:15.7	2.6	241.8	10	68	RH	5.1	0.6	0.70
110	0213:13.1	0213:18.5	1.8	291.4	6	65	LH	5.4	0.4	0.64
111	0213:50.3	0213:53.9	7.6	11.3	85	78	LHE	3.5	0.9	0.85
112	0214:31.1	0214:35.5	1.8	6.1	6	70	LH	4.4	1.0	0.78
113	0214:36.6	0214:44.0	3.9	10.8	13	72	LH	7.4	1.3	0.89
114	0214:42.4	0214:47.0	4.5	22.0	35	66	LH	4.6	1.3	0.68
115	0214:48.7	0214:52.6	1.3	45.6	15	77	LH	3.8	1.0	0.42
116	0214:52.7	0214:57.9	1.3	61.3	11	53	LH	5.2	0.9	0.97
117	0215:07.7	0215:12.1	6.3	10.6	12	51	LH	4.3	0.4	0.79
118	0215:11.1	0215:15.7	9.5	4.7	30	85	RHE	4.6	0.7	0.84
119	0215:13.7	0215:18.6	1.6	26.6	16	78	RH	4.8	0.8	0.61
120	0215:34.0	0215:37.5	8.0	17.1	25	53	LH	3.5	1.1	0.88
121	0216:04.4	0216:10.5	4.7	4.0	47	69	LH	6.0	0.9	0.82
122	0216:25.7	0216:28.3	1.4	7.7	40	77	LH	2.6	1.1	0.88
123	0216:37.4	0216:41.7	1.2	14.7	30	32	RH	4.3	1.3	0.89
124	0216:46.3	0216:49.2	2.2	9.9	70	35	RH	2.9	1.0	0.64
125	0217:09.5	0217:12.0	4.8	4.9	14	76	LH	2.5	0.5	0.92
126	0217:22.3	0217:27.1	3.5	5.2	30	67	LH	4.7	1.4	0.69
127	0217:30.7	0217:34.5	2.8	16.3	20	80	LH	3.7	0.6	0.77
128	0217:34.8	0217:38.6	1.8	67.5	5	72	LH	3.8	0.4	0.90
129	0217:56.7	0218:02.5	3.6	13.8	10	73	LHE	5.7	1.0	0.93
130	0218:22.7	0218:25.6	18.2	4.1	35	30	LHE	2.9	0.9	0.73

Table 2
(Continued)

Cycle	Start time (UT)	End time (UT)	λ_1/λ_2	λ_2/λ_3	θ_{kB_0} (deg)	$\theta_{kV_{sw}}$ (deg)	Pol.[a] (s/c)	T (sec)	Amp. (nT)	Comp.
131	0218:32.2	0218:35.2	2.9	4.7	30	64	LH	3.0	1.4	0.65
132	0218:35.3	0218:37.8	1.9	8.2	38	84	LH	2.4	0.9	0.70
133	0218:38.0	0218:40.1	1.1	12.8	47	12	LH	2.1	1.3	0.83
134	0219:00.0	0219:03.5	2.8	8.6	26	86	RH	3.5	1.6	0.75
135	0219:23.4	0219:25.5	2.2	26.7	26	89	RH	2.1	0.6	0.61
136	0219:27.6	0219:31.1	2.9	5.9	17	47	LH	3.5	1.1	0.73
137	0219:32.7	0219:34.9	9.5	10.7	37	84	LH	2.2	0.4	0.71
138	0219:38.2	0219:42.1	4.6	12.9	24	41	LH	3.8	0.9	0.73
139	0219:46.4	0219:51.3	2.7	35.6	26	47	LH	4.8	1.6	0.90
140	0220:17.6	0220:20.6	2.2	5.1	76	14	LH	3.0	1.0	0.40
141	0220:40.4	0220:43.8	6.6	8.6	28	88	LH	3.4	0.8	0.57
142	0220:45.5	0220:51.2	2.3	28.0	25	89	LH	5.7	1.1	0.95
143	0220:55.6	0220:57.3	6.0	34.7	16	74	RHE	1.6	0.2	0.66
144	0221:00.6	0221:04.2	5.9	10.8	84	45	RHE	3.5	2.7	0.94
145	0221:37.8	0221:43.2	2.7	5.6	52	45	LH	5.3	0.9	0.83
146	0221:49.0	0221:53.2	2.3	33.9	9	74	RH	4.2	0.4	0.90
147	0221:53.6	0221:58.2	1.7	10.6	18	47	RH	4.6	0.6	0.69
148	0222:07.5	0222:10.1	2.5	74.4	15	67	LH	2.5	0.4	0.87
149	0222:10.4	0222:14.9	4.3	34.4	4	59	LH	4.5	0.3	0.83
150	0222:17.8	0222:22.4	3.2	18.7	22	47	LH	4.5	0.7	0.64
151	0222:33.1	0222:39.1	8.4	13.5	29	40	RH	5.9	1.1	0.79
152	0222:41.3	0222:47.3	2.0	3.7	39	29	LH	5.9	1.3	0.70
153	0222:53.1	0222:58.6	3.2	6.4	77	41	RH	5.5	3.0	0.64
154	0223:11.2	0223:16.0	8.2	12.1	37	86	LHE	4.7	0.6	0.84
155	0223:14.8	0223:18.7	3.7	5.5	82	60	LH	3.9	0.9	0.71
156	0223:23.3	0223:29.8	1.5	20.8	65	54	RH	6.4	1.8	0.88
157	0223:46.4	0223:50.7	3.8	27.4	13	64	RH	4.2	0.6	0.88
158	0223:57.2	0223:59.9	4.9	9.8	11	52	RH	2.6	0.4	0.99
159	0224:01.5	0224:05.8	5.8	3.9	33	89	LH	4.2	0.9	0.56
160	0224:10.7	0224:15.6	2.8	6.2	79	36	RH	4.8	2.9	0.86
161	0224:41.9	0224:46.5	5.2	22.2	59	14	LH	4.6	1.4	0.78
162	0224:43.8	0224:47.7	4.1	6.8	57	28	LH	3.8	1.2	0.81
163	0224:49.1	0224:55.1	7.3	5.4	1	63	RH	5.9	0.5	0.91
164	0224:54.4	0225:02.1	5.0	11.2	1	64	LH	7.6	0.6	0.75
165	0225:02.7	0225:07.3	2.9	29.8	11	57	LH	4.6	0.4	0.81
166	0225:06.2	0225:11.6	7.3	15.2	14	52	RH	5.4	0.6	0.74
167	0225:21.2	0225:24.1	1.5	39.3	15	81	LH	2.8	0.5	0.55
168	0225:30.3	0225:34.5	2.1	40.5	4	69	LH	4.2	0.4	0.91
169	0225:41.9	0225:46.5	4.1	46.0	23	44	LH	4.6	0.74	0.89

Note. [a] LH/RH—Left/Right-hand circular, LHE/RHE—Left/Right-hand elliptical polarizations.

polarization in the spacecraft frame are given in the panels corresponding to individual cycles. As previously mentioned, the direction of the magnetic field is automatically set so that it is always "out"of the plane and is indicated by symbol *O* for each of the cycles in the figure. LH and RH indicate left-hand and right-hand polarizations, respectively. If there is nothing after the acronym, it is circularly polarized. An 'E' after the acronym means that it is elliptically polarized. The beginning and end of each wave cycle are symbolized as *begin* and *end*, respectively, to identify the clockwise or anticlockwise rotation of the wave. The waves rotating clockwise/anticlockwise relative to the ambient magnetic field are identified as RH/LH-polarized waves. It is to be noted that as the magnetic field points out of the plane in the figure, a clockwise (anticlockwise) rotation here indicates LH (RH) polarized waves.

Figure 6 gives the wave cycles for 0153:29.1–0153:33.9 UT (top left), 0154:49.3–0154:54.8 UT (top right), 0202:42.4–0202:49.1 UT (middle left), 0206:33.7–0206:40.3 UT (middle right), 0223:45.4–0223:47.1 UT (bottom left), and 0224:12.1–0224:13.4 UT (bottom right). The wave cycles shown are all LH, circularly polarized (in the spacecraft frame of reference). The waves propagate parallel/quasi-parallel ($\theta_{kB_0} < 30^\circ$) to the ambient magnetic field. There were wave cycles that were RH polarized in the spacecraft frame. More will be said about them later.

The results of the MV analysis on the *Cassini* magnetosheath waves are given in detail in Table 1. A total of 229 wave cycles have been analyzed, and the events are numbered chronologically. The table highlights the major features of the wave cycles. The second and third columns are the start and end times of each analyzed interval. The fourth and fifth columns give the λ_1/λ_2 and λ_2/λ_3 ratios, respectively. The sixth and seventh columns are the wave propagation angles θ_{kB_0} and $\theta_{kV_{sw}}$, the angle of $\boldsymbol{k}$ relative to the ambient magnetic field B_0 and to the solar wind direction $\boldsymbol{V}_{sw}$, respectively. The eighth column is the wave polarization. The next three columns give the wave period (in seconds), wave amplitude (in nT), and wave compression, respectively.

It can be noticed that the wave cycles are mostly LH polarized in the spacecraft frame. The waves propagate in a varied range of θ_{kB_0} values. Most of the waves are found to be circularly

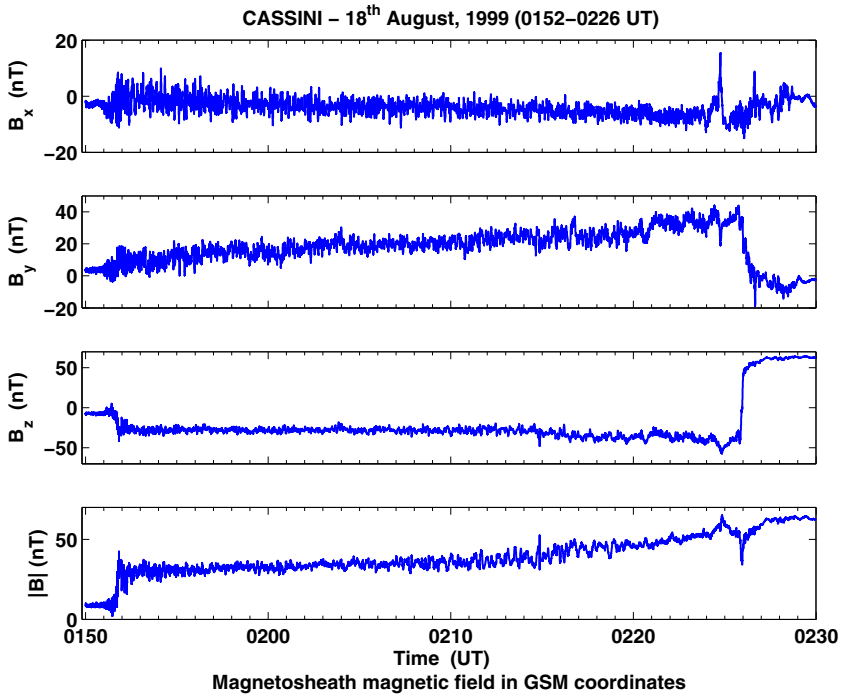

Figure 3. *Cassini*: temporal behavior of the Earth's magnetosheath magnetic field in GSM coordinates. The bow shock (∼0151:50 UT) and the magnetopause (∼0226:00 UT) crossings are also shown.

(A color version of this figure is available in the online journal.)

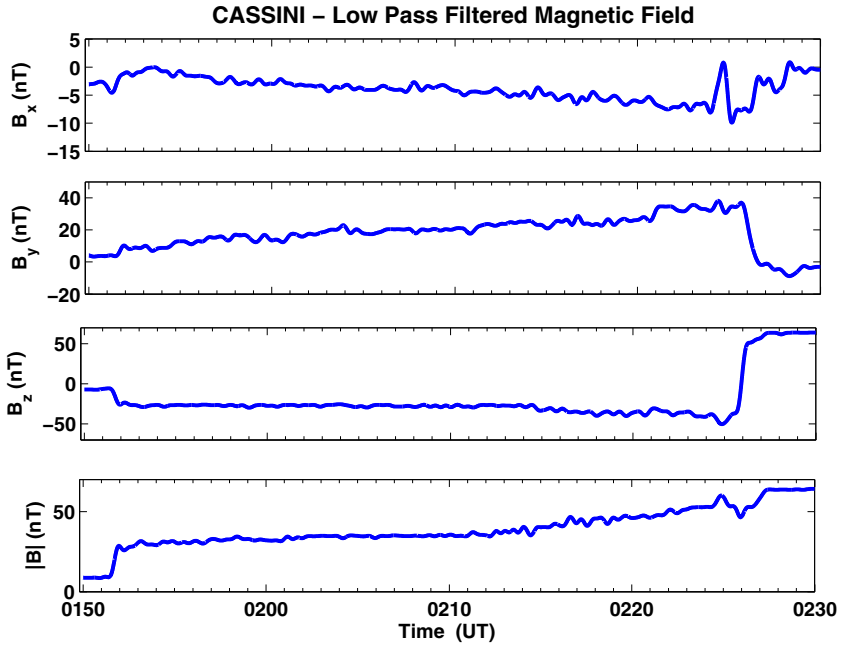

Figure 4. *Cassini*: background magnetic field obtained after a low-pass filtering of the raw data at 30 mHz.

(A color version of this figure is available in the online journal.)

polarized even at highly oblique propagation angles (e.g., see cycles 61, 113, and 154). An example is shown in Figure 7 that corresponds to cycle 61 of Table 1. About 80% (183/229) of the wave cycles are LH polarized and ∼20% are RH polarized in the spacecraft frame. No wave cycles were found that were linearly polarized.

The observed waves were found to have frequencies less than or close to the ion (proton) cyclotron frequency (f_p) in the spacecraft frame and hence were probably propagating in the ion (proton) cyclotron mode. The few that were detected at values above f_p will be discussed further later.

The waves analyzed were found to be compressional, which means that the magnetic field magnitude changed across their structures. The compression factors as described above varied between 0.2 and 1.0. The causes of the compression are beyond the scope of the present work.

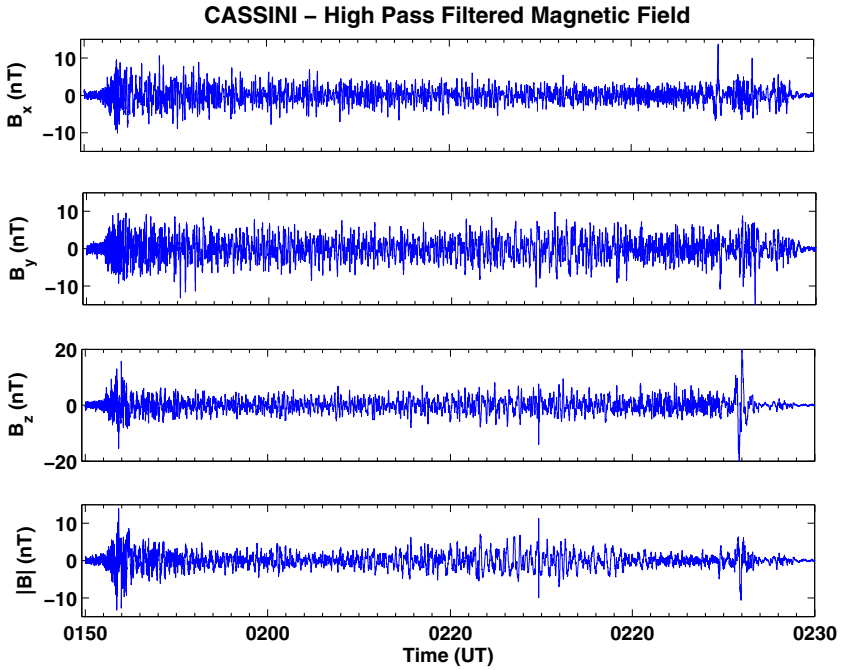

Figure 5. *Cassini*: magnetosheath wave fields obtained from *Cassini* after the removal of low-pass data.
(A color version of this figure is available in the online journal.)

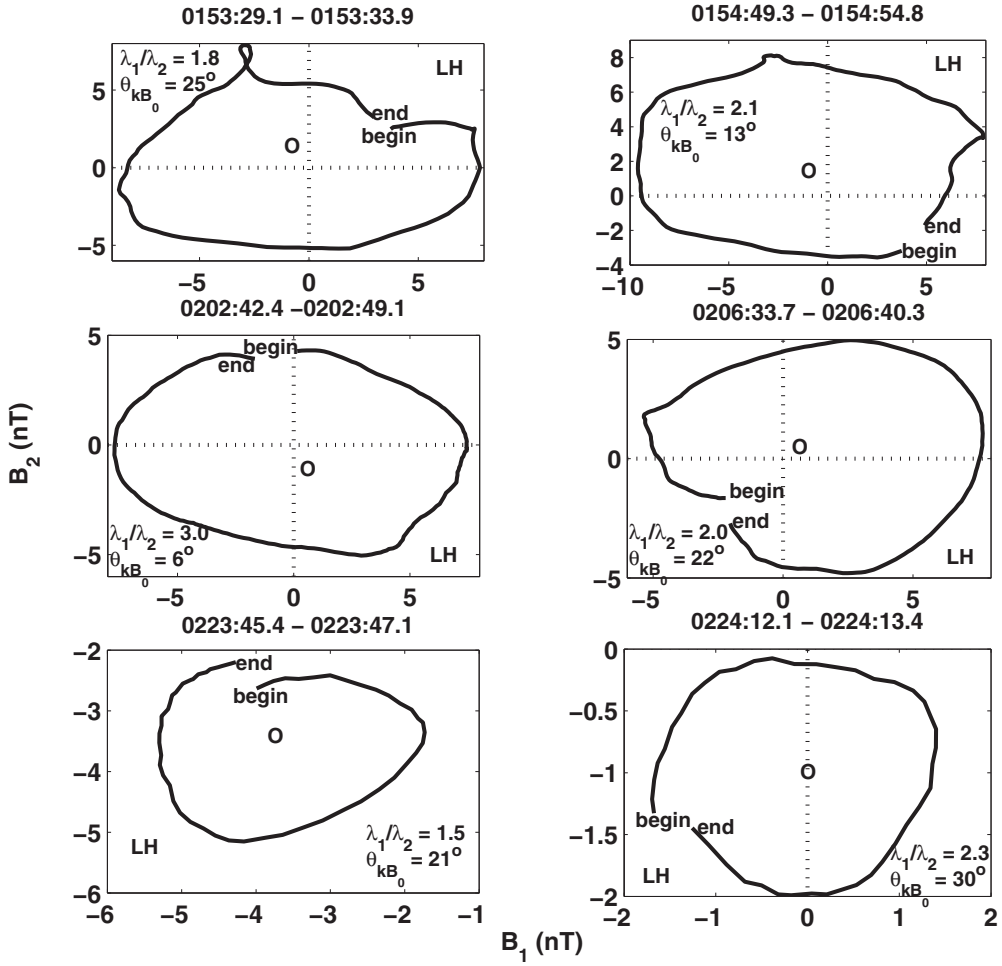

Figure 6. *Cassini*: hodograms of the magnetosheath wave cycles in minimum variance coordinates for the interval 0152–0226 UT.

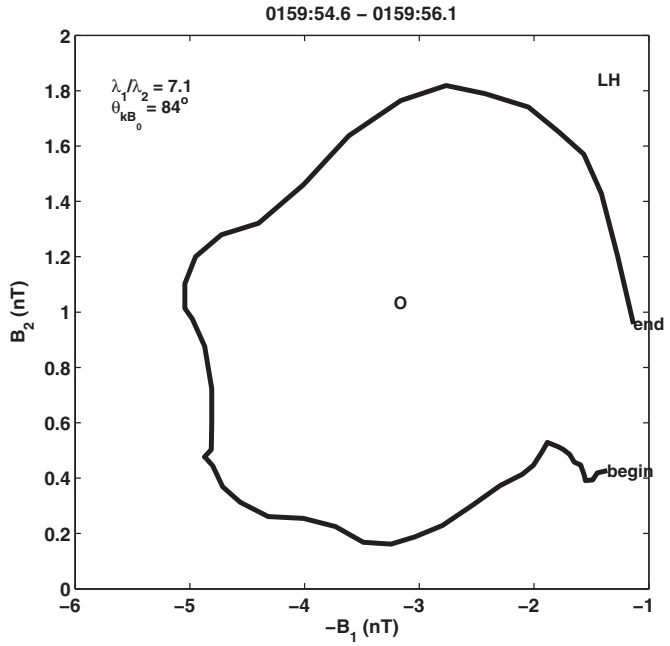

Figure 7. Hodogram for the *Cassini* data interval 0159:54.6–0159:56.1 UT (cycle 61 of Table 1), indicating a highly oblique circularly polarized wave.

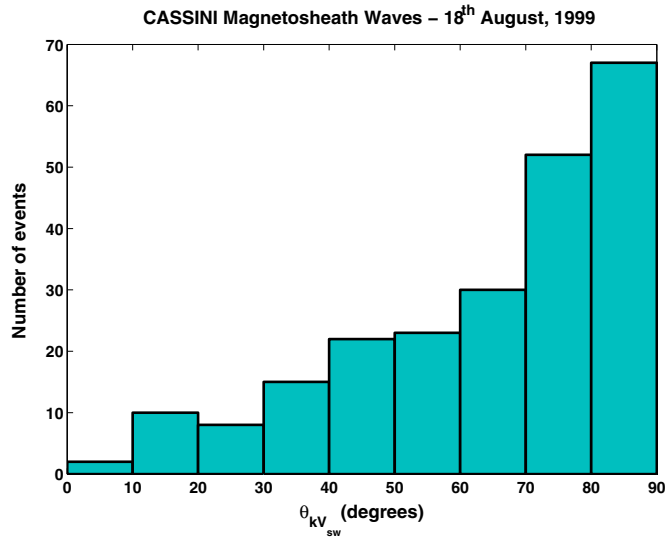

Figure 8. *Cassini*: histogram of the magnetosheath wave propagation directions with respect to the solar wind flow direction.

(A color version of this figure is available in the online journal.)

3.1.2. Wave Intrinsic Polarization

Figure 8 shows the distribution of the wave events over the wave propagation direction $\theta_{kV_{sw}}$ with respect to the solar wind flow velocity. It can be seen that about 50% of the waves propagate almost orthogonal to the solar wind flow velocity. This can be explained by the geometry of the magnetic field in the magnetosheath. The magnetosheath magnetic field is almost orthogonal to the plasma flow direction (see Figure 4). Thus waves traveling parallel to the ambient magnetic field will be propagating nearly orthogonal to the magnetosheath plasma flow.

We identified the waves that were propagating at angles greater than 75° to the magnetosheath flow velocity V_{sw}. These waves were propagating almost orthogonal to the flow and would not be Doppler shifted much in either their frequency or

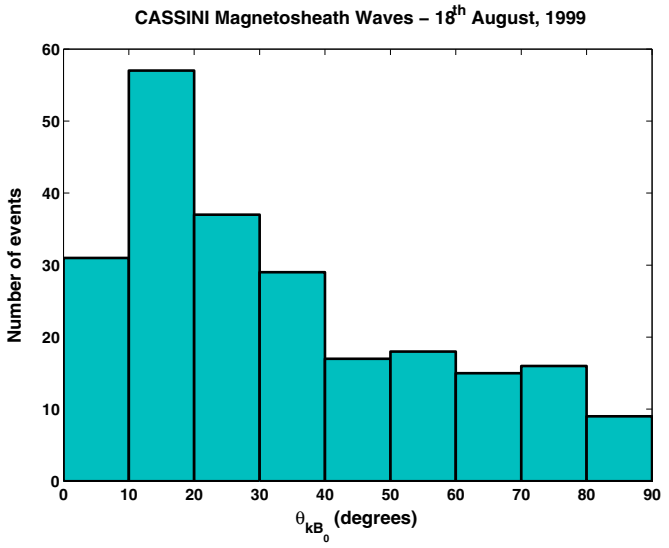

Figure 9. *Cassini*: distribution of the magnetosheath wave propagation directions with respect to the background magnetic field.

(A color version of this figure is available in the online journal.)

sense of polarization. So those waves detected as LH polarized in the spacecraft frame would be LH polarized in the plasma frame. The solar wind flow velocity is assumed to be in the $-x$ direction, and the events with $\theta_{kV_{sw}} > 75°$ are examined from *Cassini* wave events (Table 1). We find that 81 out of 94 waves in this angular range (75° to 90°) were indeed LH polarized in the plasma frame.

We performed an additional analysis on all RH waves. Because there is a 180° ambiguity in the wave $\boldsymbol{k}$ direction, we cannot determine (without the electric field component of the waves) whether the wave has an upstream direction component or a downstream direction component. Waves that are flowing upstream (against the flow of the solar wind) could be anomalously Doppler-shifted such that their sense of polarization in the plasma frame is reversed from what they are in the spacecraft frame. Thus we have checked all RH waves to see if their theoretical phase speed components in that direction are less than V_{sw}. If the components are less than V_{sw}, then the waves detected in the spacecraft frame as RH could be intrinsically LH.

There were 46 wave events that were identified as RH in our study. We calculate the proton cyclotron wave phase velocity from the measured plasma conditions. The speed is $V_{ph} = 190$ km s^{-1}. The V_{sw} is 436 km s^{-1}. We consider the inequality $V_{ph} \cos \theta_{kVsw} < V_{sw}$. When tested, all 46 of the RH waves were found to have phase speed components less than the magnetosheath flow speed. Therefore it is possible that all RH waves in the spacecraft frame were LH polarized in the plasma frame.

3.1.3. Wave Statistics

Figures 9 and 10 sum up the statistical results of the *Cassini* magnetosheath wave analysis. A histogram of θ_{kB_0} is presented in Figure 9. The waves propagate at all angles with about 55% of wave cycles having $\theta_{kB_0} < 30°$, 28% with $30° < \theta_{kB_0} < 60°$, and 17% with $\theta_{kB_0} > 60°$. As mentioned earlier, the majority of the waves were circularly polarized even at $\theta_{kB_0} > 60°$.

Figure 10 depicts the histogram of the wave frequency normalized to proton gyrofrequency $\Omega_p = 2\pi f_p$ (top panel) and the dependence of θ_{kB_0} on the normalized wave frequency

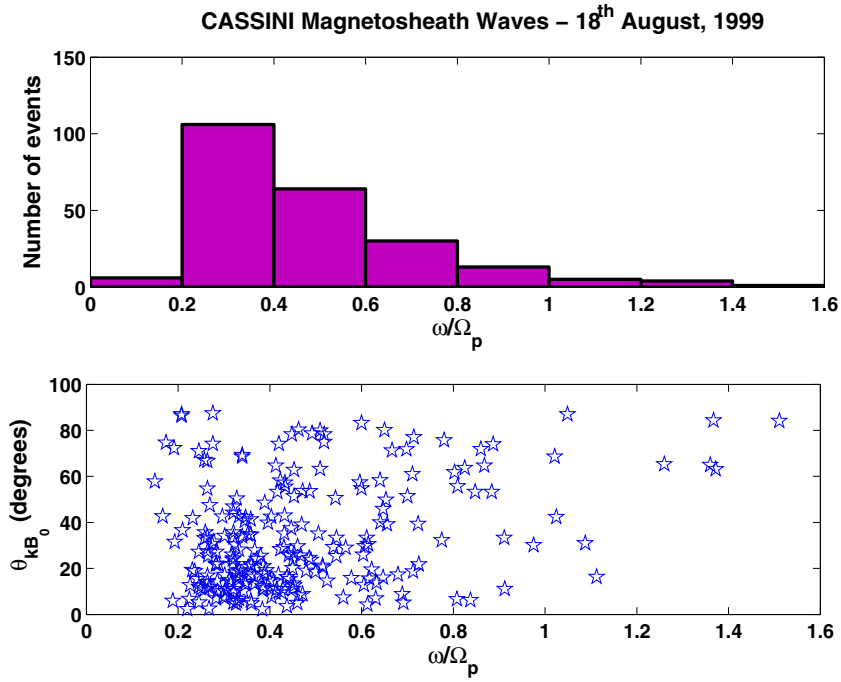

Figure 10. *Cassini*: histogram of the wave frequencies normalized to proton cyclotron frequency ω/Ω_p (top panel) and dependence of propagation angle on the normalized wave frequencies (bottom panel).

(A color version of this figure is available in the online journal.)

(bottom panel). Almost all of the waves had frequencies less than the proton gyrofrequency with maximum distribution around half of the proton gyrofrequency ($\Omega_p/2$) (Southwood et al. 2001; Tsurutani et al. 2002a; Bogdanov et al. 2003). Ten out of a total of 229 events were found to have frequencies above the proton gyrofrequency ($\omega/\Omega_p > 1$). If these wave events were propagating in the magnetosheath flow direction, they would remain LH polarized and would be Doppler shifted to higher frequencies. To analyze these events for Doppler shift in frequency, we calculate the plasma frame frequency for each wave cycle assuming that the waves were propagating downstream and were Doppler shifted upward in frequency. We use the Doppler-shift relation (Tsurutani et al. 1983)

$$f_{\rm scf} = f_{pf}\left(1 + \frac{V_{sw}}{V_{ph}}\cos\theta_{kV_{sw}}\right), \quad (1)$$

where $f_{\rm scf}$ and f_{pf} are the frequencies in the spacecraft frame and plasma frame, respectively. It was found that 9 out of the 10 events with $\omega/\Omega_p > 1$ had frequencies f_{pf} less than the proton gyrofrequency. Therefore, it is possible that the waves with $f_{\rm scf} > f_p$ have intrinsic frequencies $< f_p$ and have been Doppler shifted upward by the magnetosheath flow.

The scatter plot in the bottom panel of Figure 10 does not render any peculiar trend. Still, the majority of the waves with propagation angles $\theta_{kB_0} < 40^\circ$ seem to have $\omega/\Omega_p < 0.5$.

Figure 11 is an effort to quantify the coherence of the *Cassini* waves. The figure shows the $B_1 - B_2$ components of *Cassini* waves for the time interval 0201:04.8–0203:06.1. The top panel shows the B_1 and B_2 values as a function of time. The bottom panel shows the $B_1 - B_2$ cross-correlation result. For the *Cassini* waves, the peak correlation coefficient is 0.72 at $\lambda/4$ lag and falls off with greater lags. The correlation coefficient is ~0.3 at ± one lag. In comparison to the magnetospheric chorus at the equator (Tsurutani et al. 2011a), we would say that the *Cassini* magnetosheath ion cyclotron waves are quasi-coherent.

3.2. Observational Results from WIND

The *WIND* magnetometer observations provided magnetic vector measurements at 11 samples per second. The magnetic field components in GSE coordinates for the interval 0152–0226 UT are portrayed in Figure 12. The magnetic field magnitude increases toward the magnetopause due to the field line draping effect that is evident from the figure. Here again the raw data is low-pass filtered at 15 mHz frequency (obtained empirically for *WIND* data) to obtain the ambient field data. The high-pass filtered data is then used to study the wave fluctuations. Figures 13 and 14 display the low-pass ambient magnetic field and the remainder high-pass wave fields, respectively. Here again, Figure 13 indicates that the magnetosheath magnetic field is directed primarily orthogonal to the Sun–Earth line. It is evident from the figures that the fluctuations are ~2 nT in a ~22 nT field, comparatively smaller than that of *Cassini*.

3.2.1. Wave Events

The MVA are applied to individual wave cycles from the *WIND* high-pass filtered field data. Figure 15 illustrates examples of the minimum variance analysis results performed on various wave cycles. Various parameters like θ_{kB_0}, UT, polarization in the spacecraft frame, and the direction of the ambient magnetic field (out of plane) are indicated on each of the figures. The notation LH(E)/RH(E) represents LH/RH circular (elliptical) polarizations. The words *begin* and *end* in each figure point to the beginning and end of each wave cycle.

Figure 15 illustrates the wave cycles 0155:54.8–0156:00.3 UT, 0202:48.7–0202:50.9 UT, 0208:01.3–0208:06.6 UT, 0214:48.7–0214:52.6 UT, 0224:41.9–0224:46.5 UT, and 0224:43.8–0224:47.7 UT. All wave cycles in the hodograms have the ambient field out of the plane and show LH circularly polarized waves. For the wave event 0155:54.8–0156:00.3, the propagation angle is $\theta_{kB_0} = 89^\circ$ and is still more or less circularly polarized.

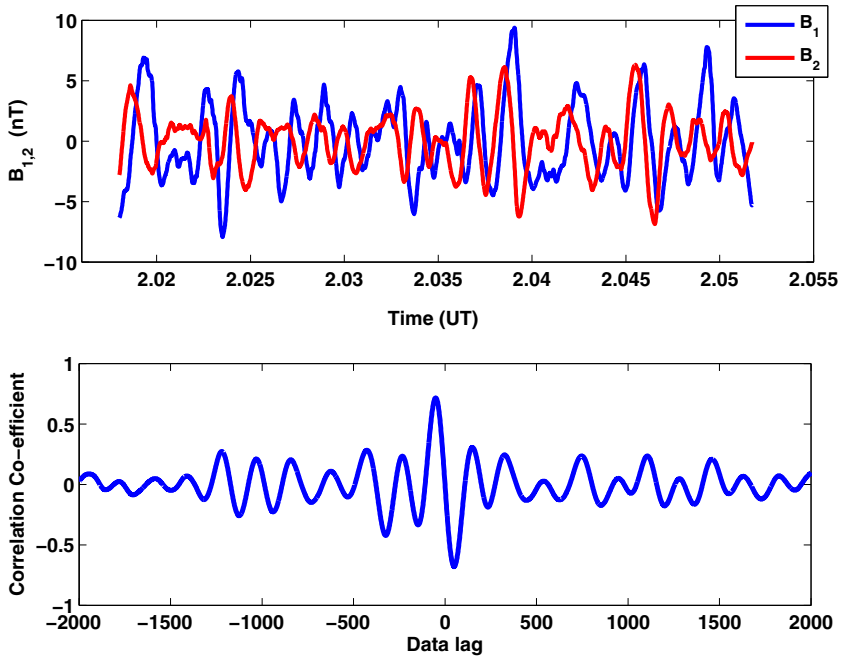

Figure 11. $B_1 - B_2$ components of *Cassini* waves for the interval 0201:04.8–0203:06.1 (top panel). The correlation coefficient at various data point lags are indicated in the bottom panel. Peak correlation coefficient is 0.72 at lag −51.

(A color version of this figure is available in the online journal.)

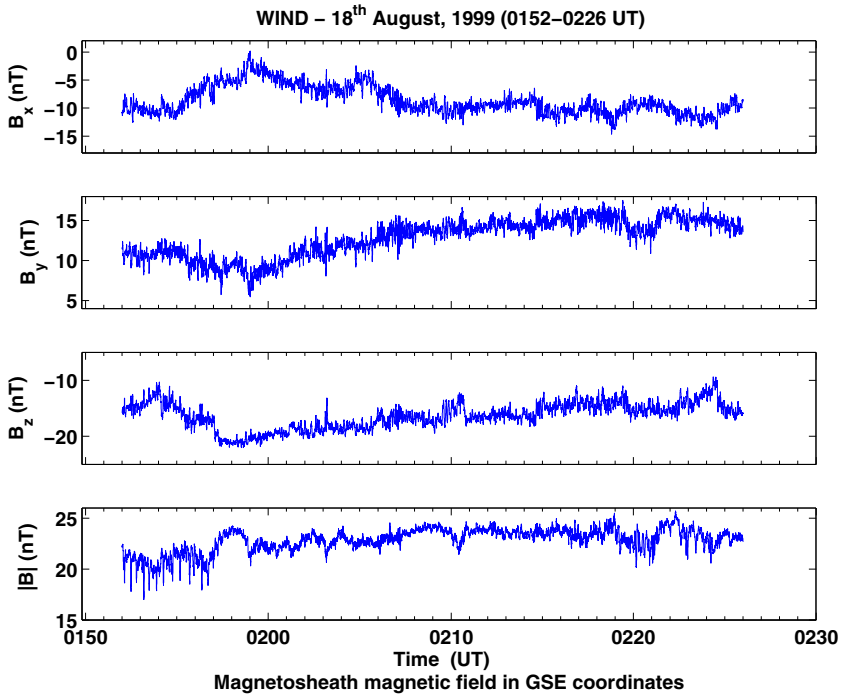

Figure 12. *WIND*: temporal behavior of the Earth's magnetosheath magnetic field in GSE coordinates for the interval 0152–0226 UT.

(A color version of this figure is available in the online journal.)

The *WIND* magnetosheath wave results are given in Table 2. The format is identical to that of Table 1; 169 cycles have been analyzed in total and are given chronologically in the table. The *WIND* waves are typically LH circularly polarized. The waves are found to be circularly polarized even at highly oblique propagation angles (cycle 0155:54.8–0156:00.3 in 15). About 76% of the waves have LH polarization, and ∼24% are RH polarized in the spacecraft frame. Again, no waves were found to have linear polarization.

3.2.2. Wave Intrinsic Polarization

Wave events from *WIND* data (Table 2) are examined to identify cases with wave propagation direction nearly orthogonal to the solar wind direction. The *WIND* plasma velocity data are used to find the angle $\theta_{kV_{sw}}$, and a histogram of the angle $\theta_{kV_{sw}}$ is shown in Figure 16. Fifty-nine events were observed to have $\theta_{kV_{sw}} > 75^\circ$, and 85% (50/59) of these wave cycles were found to be LH polarized.

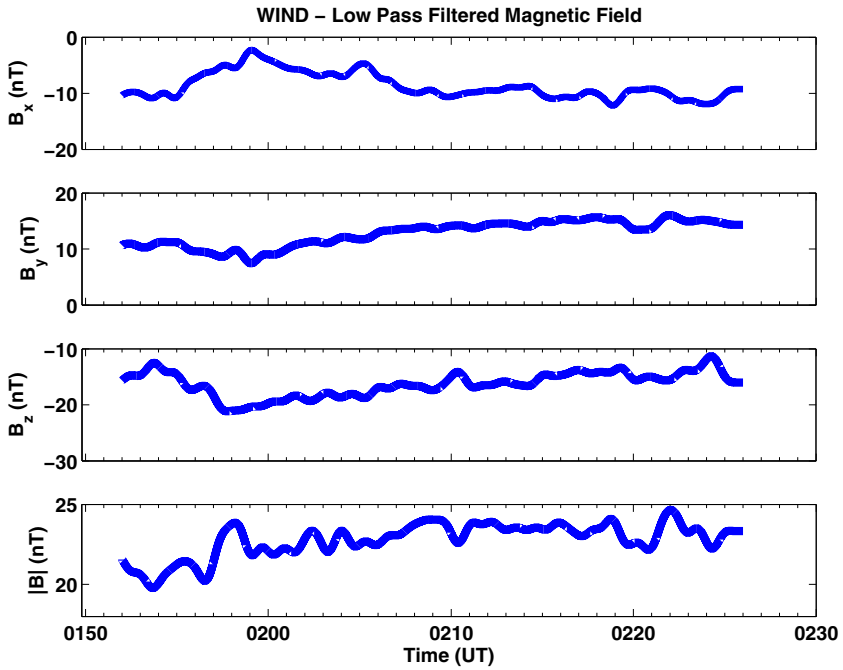

Figure 13. *WIND*: background magnetic field obtained after a low-pass filtering of the raw data at 15 mHz.
(A color version of this figure is available in the online journal.)

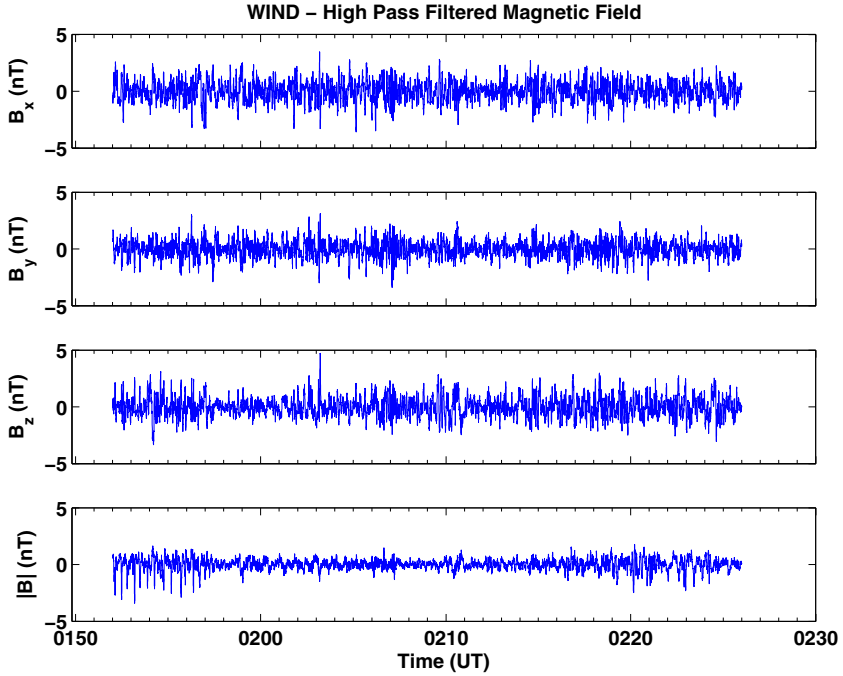

Figure 14. *WIND*: magnetosheath wave fields obtained after the removal of low-pass data.
(A color version of this figure is available in the online journal.)

Further, we reexamine the RH-polarized waves to identify cases that might have been anomalously Doppler shifted. Under the supposition that the RH waves have an upstream component, we check to see if the wave speed component in the direction of V_{sw} is less than V_{sw}. We have 41 *WIND* wave events that are RH polarized in the spacecraft frame. Using the measured plasma conditions at the magnetosheath, we obtain the wave phase velocity $V_{ph} = 190$ km s^{-1} and apply it in the inequality $V_{ph} \cos\theta_{kVsw} < V_{sw}$. All of the RH-polarized waves were found to have phase speed components less than the magnetosheath flow speed. Therefore it is possible that all of these RH wave events were LH polarized in the plasma frame and anomalously Doppler shifted to the RH in the spacecraft frame.

3.2.3. Wave Statistics

Figures 17 and 18 summarize the statistical results of the *WIND* magnetosheath wave analysis. A histogram of the wave propagation angle θ_{kB_0} is exhibited in Figure 17. The waves propagate at all angles with more than 64% being propagated at $\theta_{kB_0} < 30^\circ$ with respect to the background magnetic field

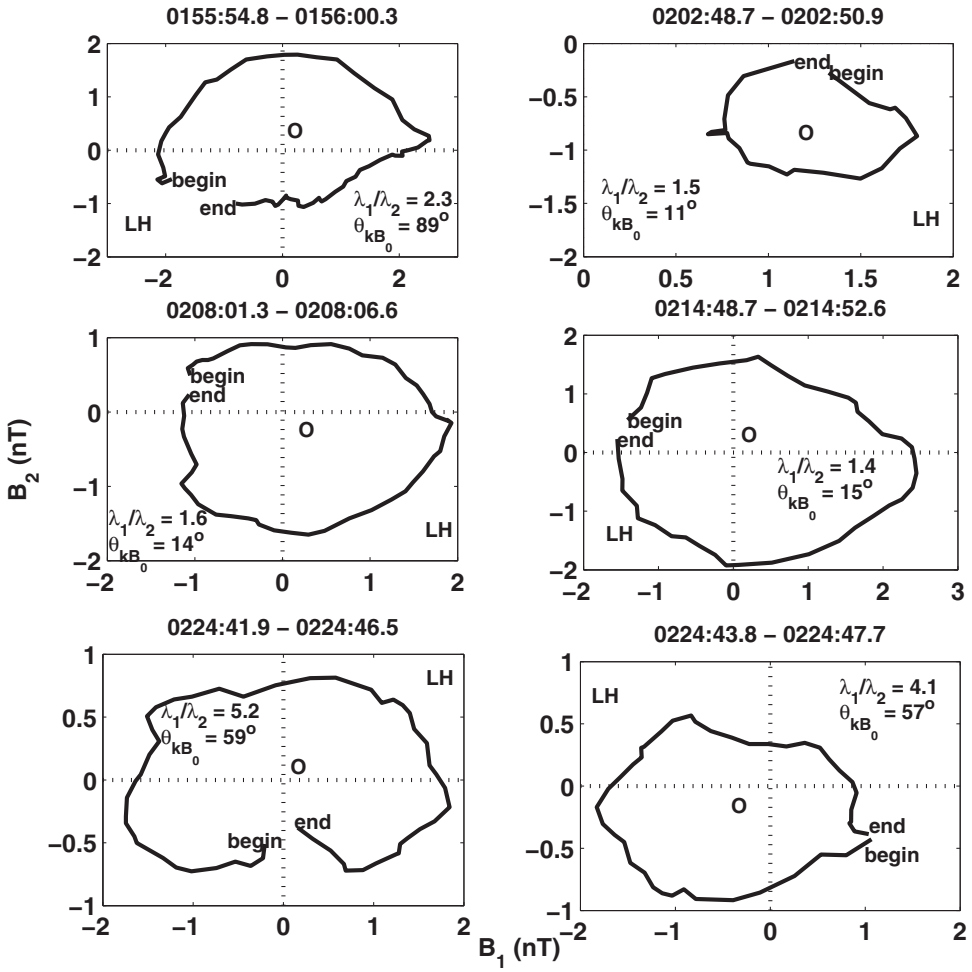

Figure 15. *WIND*: hodograms of the magnetosheath wave cycles in minimum variance coordinates for the interval 0152–0226 UT.

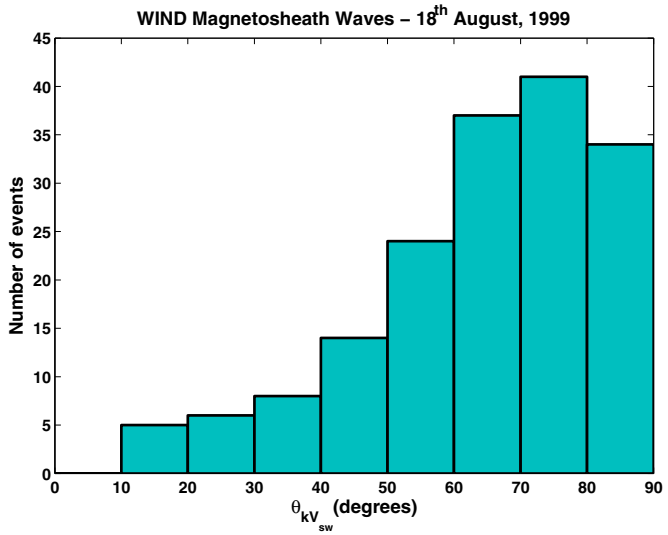

Figure 16. *WIND*: histogram of the magnetosheath wave propagation directions with respect to the solar wind velocity.

(A color version of this figure is available in the online journal.)

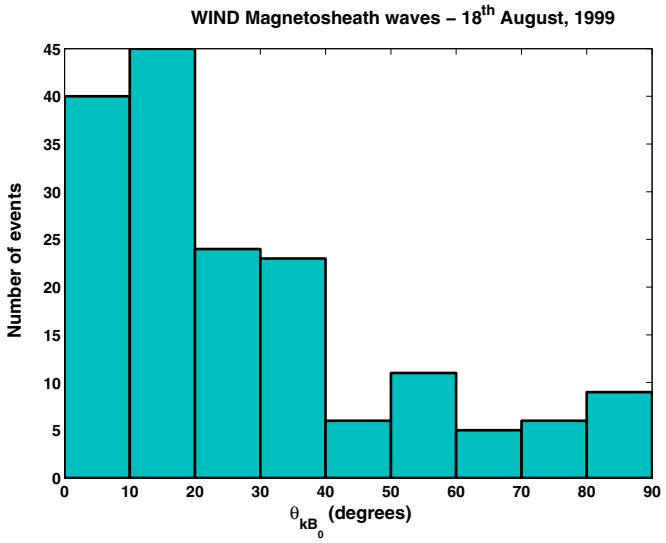

Figure 17. *WIND*: distribution of the magnetosheath wave propagation directions with respect to the background magnetic field.

(A color version of this figure is available in the online journal.)

$\boldsymbol{B}$. Some 24% of the waves propagate at $30^\circ < \theta_{kB_0} < 60^\circ$, and around 12% (20/169) of the waves show a high tendency toward being highly oblique $\theta_{kB_0} > 60^\circ$. Even at highly oblique propagation angles, the waves were found to be circularly polarized (see cycles 22, 36, and 41 in Table 2).

Figure 18 shows a histogram of the wave frequency, normalized to proton gyrofrequency (top panel), and the scatter plot of the normalized wave frequency as a function of θ_{kB_0} (bottom panel). The *WIND* waves have frequencies less than

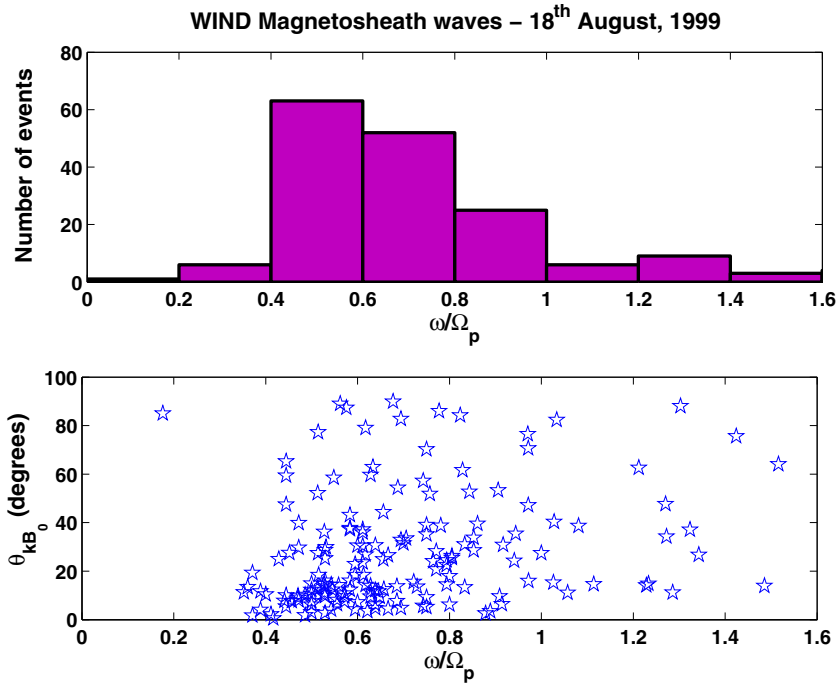

Figure 18. *WIND*: histogram of the wave frequencies normalized to proton cyclotron frequency ω/Ω_p (top panel) and dependence of propagation angle on the normalized wave frequencies (bottom panel).

(A color version of this figure is available in the online journal.)

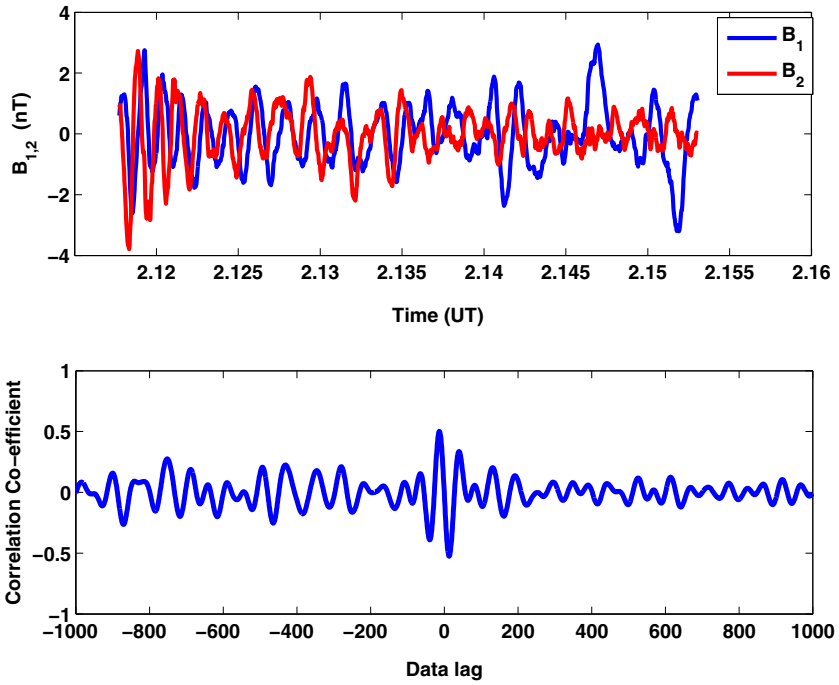

Figure 19. $B_1 - B_2$ components of *WIND* waves for the interval 0207:03.7–0209:10.8 (top panel). The correlation coefficient at various data point lags are indicated in the bottom panel. Peak correlation coefficient is 0.52 at lag −13.

(A color version of this figure is available in the online journal.)

the proton gyrofrequency with a maximum distribution around or less than half the proton gyrofrequency ($\Omega_p/2$). Here, 22 out of 169 events were observed to have frequencies above the proton gyrofrequency ($\omega/\Omega_p > 1$). To examine whether these events were Doppler shifted in frequency, we calculate the plasma frame frequency for each wave event with the assumption that the waves had a downstream propagation component. Assuming that these waves had a component of propagation in the magnetosheath flow direction and using the Doppler-shift relation of Equation (1), it was found that 17 out of 22 events with $\omega/\Omega_p > 1$ had frequencies f_{pf} less than the proton gyrofrequency. Therefore, it is inferred that the waves have been Doppler shifted to higher frequencies in the spacecraft frame by the magnetosheath flow.

The bottom panel of Figure 18 does not show any specific trend. As in the case of *Cassini* waves, the majority (65%) of

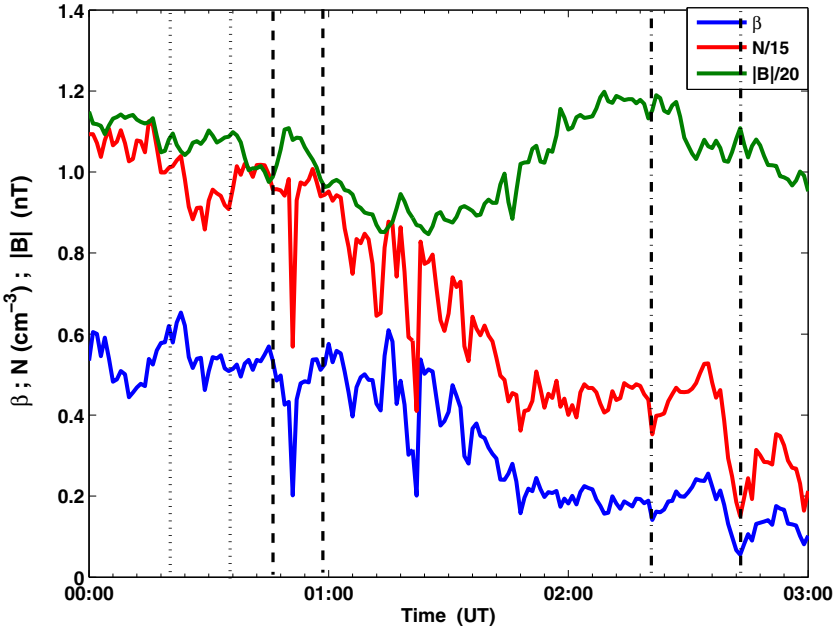

Figure 20. Variation of plasma beta β, plasma number density N, and the magnetic field magnitude $|B|$ along the trajectory of *WIND* in the magnetosheath (0000–0300 UT). The plasma number density and the magnetic field values are divided by a factor of 15 and 20, respectively, to fit into the scale. The black vertical lines highlight the regions where an anticorrelation in the density and magnetic field signature is visible.

(A color version of this figure is available in the online journal.)

the waves with propagation angles $\theta_{kB_0} < 30^\circ$ were found to have values $\omega/\Omega_p < 0.8$.

Figure 19 quantifies the coherence of the *WIND* waves. The top panel of the figure shows the $B_1 - B_2$ components of *WIND* waves for the time interval 0207:03.7–0209:10.8 as a function of time. The bottom panel shows the $B_1 - B_2$ cross-correlation result. The peak correlation coefficient is 0.52 for the *WIND* waves at $\lambda/4$ lag and falls off with greater lags. The correlation coefficient is ∼0.32 at ± one lag. Consistent with the *Cassini* waves, the *WIND* ion cyclotron waves are also found to be quasi-coherent.

3.3. Cyclotron Wave Occurrence: A Plausible Explanation

This section is an attempt to give a possible explanation for the unusual occurrence of the proton (ion) cyclotron waves in the Earth's magnetosheath region where mirror modes are usually the dominant wave structures (Tsurutani et al. 1982, 1984; Soucek et al. 2008; Horbury & Lucek 2009; Soucek & Escoubet 2011).

During the *Cassini* Earth flyby, the interplanetary magnetic field (IMF) was ∼70° relative to V_{sw}, which means that the subsolar shock was quasi-perpendicular. That would mean that compression at the shock would give proton anisotropies needed for the growth of either electromagnetic ion cyclotron or mirror-mode waves. Also, due to the nearly orthogonal orientation of the IMF, magnetic field line draping (Midgley & Davis 1963; Zwan & Wolf 1976) should also add to the free energy for the instabilities as the plasma and fields convect toward the magnetopause.

Figure 20 illustrates the temporal variation of the total plasma beta β (blue curve), plasma density N (red curve), and the magnetic field magnitude (green curve) over the interval 0000–0300 UT when *WIND* was in the magnetosheath. Here β is the ratio of the plasma kinetic to magnetic pressure. The pairs of black vertical lines indicate the time intervals where the plasma density and magnetic field magnitude were anticorrelated. It can be noticed that the ion beta was very low (mean $< \beta >= 0.35$) throughout the magnetosheath passage, which favors the proton (ion) cyclotron waves, according to previous theoretical studies (Gary 1992) and observational evidence (see Schwartz et al. 1996 and references therein). Further, at such low β values, the mirror-mode oscillations would need very high proton temperature anisotropy to grow, if at all. Therefore, it seems plausible to deduce that the significantly low value of β could have been a possible reason for the highly unusual occurrence of proton cyclotron waves in the Earth's magnetosheath.

4. DISCUSSION AND CONCLUSIONS

During the *Cassini* encounter with the Earth, an interplanetary high-speed solar wind stream ($<V_{sw}> = 598$ km s^{-1}) (Tsurutani et al. 2002a) impinged upon the bow shock. The upstream interplanetary magnetic field was nearly orthogonal to the solar wind flow, so the subsolar bow shock was quasi-perpendicular, leading to a magnetosheath ion anisotropy with $T_{\perp i}/T_{\parallel i} > 1$, which is unstable to both the mirror-mode and the ion cyclotron instabilities. However, it is shown in this work that the magnetosheath had an unusually low plasma beta ∼0.35 during this interval. As indicated from theoretical studies (Price et al. 1986; Gary 1992; Gary et al. 1993; Remya et al. 2013), in such circumstances, the proton cyclotron instability will dominate over the mirror instability. This is exactly what is found. The entire magnetosheath appeared to be filled with transverse electromagnetic waves.

From a new method of wave analysis, it is shown that the majority of the waves were observed to be LH polarized with frequencies below f_p. This is in the spacecraft frame. For the minority of events that are noted to be RH polarized and to have spacecraft frame frequencies $> f_p$, additional tests were made. It is found that both of these categories of events were consistent with their being LH waves with frequencies $< f_p$ in the plasma frame. We thus conclude that the waves detected at both *Cassini* and *WIND* are electromagnetic

LH-polarized proton cyclotron waves. There is no evidence of mode conversion to (plasma frame) RH waves, even though the wave amplitudes are exceptionally large (∼10 nT).

The majority of the waves are propagating parallel to B_0 and are circularly polarized. This is expected from linear theory. However, it is also found that for waves propagating at oblique angles to B_0, the polarization is still circularly polarized. This is not understood at this time. It is possible that ion cyclotron waves should be circularly polarized at all angles of propagation, but to the authors' knowledge this has not been demonstrated by theory yet. It should be noted that in a parallel work Verkhoglyadova et al. (2010) examined whistler-mode waves (magnetospheric chorus and plasmaspheric hiss) and showed that they should be circularly polarized independent of direction of propagation. A similar work is needed for ion cyclotron waves.

The proton cyclotron waves are shown to be compressive, with a maximum factor of 1.0 found. At this time we do not have an explanation for this feature of the waves. Several possibilities exist. It could be due to something as simple as oblique propagation leading to a magnetic component of the wave lying along B_0. Another possibility is that wave–wave interaction is taking place. A third possibility is that wave phase steepening and dissipation are taking place. The latter possibility has been shown to occur for cometary waves (Tsurutani et al. 1987, 1989) and for interplanetary Alfven waves (Tsurutani et al. 2002b, 2006). Further efforts need to be made in this direction. However, this is beyond the scope of the present paper.

The proton cyclotron waves detected at both *Cassini* and *WIND* are found to be quasi-coherent. This has important implications for the isotropization/thermalization of the magnetosheath ions. If the present case is similar to magnetospheric energetic electrons (Lakhina et al. 2010; Tsurutani et al. 2011a), then the ions should be rapidly transported in the pitch angle.

5. FINAL COMMENTS

Although this is only one case showing that the ion cyclotron instability dominates in the Earth's magnetosheath during a low-β case, it is in agreement with linear theory, and we can expect further verification if specific cases of low-β intervals are studied in the future. This should also be the case for all planetary magnetosheaths and the heliosheath as well.

The coherence of ion cyclotron waves in the Earth's magnetosphere has not been studied to date. The waves in this low-β plasma region will not be contaminated by the general turbulence ever-present in the magnetosheath and may show greater coherence than found in the magnetosheath. Ion cyclotron (called electromagnetic ion cyclotron or EMIC by the magnetospheric community) waves can have anomalously Doppler-shifted cyclotron resonance with relativistic electrons. In this wave–particle interaction, the right-hand electrons overtake the left-hand waves such that the electrons sense the waves as right-handed in its frame (see Thorne & Kennel (1971) and Tsurutani & Lakhina (1997) for more details). This wave–particle mechanism has been embraced by the radiation belt community as being a possible important source of relativistic electron loss (Horne & Thorne 1998; Summers et al. 1998; Horne et al. 2009; Shprits et al. 2009; Ni & Summers 2010; Chen et al. 2013). Omura & Zhao (2012, 2013) have theoretically examined the effects of coherent EMIC waves. However, to date, the level of coherence of EMIC waves has not been examined nor has this feature been incorporated in magnetospheric models. Thus, if magnetospheric ion cyclotron waves are found to be coherent, this will alter the possible role of these waves in the loss of relativistic electrons.

B. Remya thanks the Indian Institute of Geomagnetism, Navi Mumbai, India, for providing her with a Senior Research Fellowship and subsequently a Research Associateship to carry out this research work. Portions of this research were performed at the the Jet Propulsion Laboratory, California Institute of Technology under contract with NASA. G.S.L. thanks the National Academy of Sciences, India (NASI), for the support under the NASI-Senior Scientist Platinum Jubilee Fellowship. E.E. acknowledges CNPQ agency contract 301233/2011-0 and FAPESP agency contract 2012/06673-4 for support for this work. The work of K.H.G. was financially supported by the German Bundesministerium fuer Wirtschaft und Technologie and the Deutsches Zentrum fuer Luft- und Raumfahrt under contract 50QP1001.

REFERENCES

Anderson, B. J., & Fuselier, S. A. 1993, JGR, 98, 1461
Anderson, B. J., Fuselier, S. A., Gary, S. P., & Denton, R. E. 1994, JGR, 99, 5877
Bogdanov, A. T., Glassmeier, K.-H., Musmann, G., et al. 2003, AnGeo, 21, 2043
Chandrasekhar, S., Kaufman, A. N., & Watson, K. M. 1958, Proc. R. Soc. London, Ser. A, 245, 435
Chen, L., Thorne, R. M., Shprits, Y., & Ni, B. 2013, JGR, 118, 2185
Chisham, G., Burgess, D., & Schwartz, S. J. 1998, JGR, 103, 26765
Chisham, G., Schwartz, S. J., Balikhin, M. A., & Dunlop, M. W. 1999, JGR, 104, 437
Constantinescu, O. D., Glassmeier, K.-H., Motschmann, U., et al. 2006, JGR, 111, A09221
Constantinescu, O. D., Glassmeier, K.-H., Treumann, R., & Fornacon, K.-H. 2003, GeoRL, 30, 1802
Dunlop, M. W., Lucek, E. A., Kistler, L. M., et al. 2002, JGR, 107, 1228
Gary, S. P. 1992, JGR, 97, 8519
Gary, S. P., Fuselier, S. A., & Anderson, B. J. 1993, JGR, 98, 1481
Glassmeier, K.-H., & Neubauer, F. M. 1993, JGR, 98, 20921
Glassmeier, K.-H., Neubauer, P. M., Acuna, M. H., & Mariani, F. 1987, A&A, 187, 65
Glassmeier, K.-H., Richter, I., Diedrich, A., et al. 2007, SSRv, 128, 649
Hasegawa, A. 1969, PhFl, 12, 2642
Hasegawa, A. 1975, Plasma Instability and Nonlinear Effects (New York: Springer)
Hasegawa, A., & Tsurutani, B. T. 2011, PhRvL, 107, 245005
Horbury, T. S., & Lucek, E. A. 2009, JGR, 114, A05217
Horbury, T. S., Lucek, E. A., & Balogh, A. 2004, JGR, 109, A09209
Horne, R. B., Lam, M. M., & Green, J. C. 2009, GeoRL, 36, L19104
Horne, R. B., & Thorne, R. M. 1998, GeoRL, 25, 3011
Kennel, C. F., & Petschek, H. E. 1966, JGR, 71, 1
Khan, H., Cowley, S. W. H., Kolesnikova, E., et al. 2001, JGR, 106, 30141
Lacombe, C., Pantellini, F. G. E., Hubert, D., et al. 1992, AnGeo, 10, 772
Lakhina, G. S., Tsurutani, B. T., Verkhoglyadova, O. P., & Pickett, J. S. 2010, JGR, 115, A00F15
Lucek, E. A., Dunlop, M. W., Balogh, A., et al. 1999a, AnGeo, 17, 1560
Lucek, E. A., Dunlop, M. W., Balogh, A., et al. 1999b, GeoRL, 26, 2159
Lucek, E. A., Dunlop, M. W., Horbury, T. S., et al. 2001, AnGeo, 19, 1421
Midgley, J. E., & Davis, L., Jr. 1963, JGR, 68, 5111
Narita, Y., & Glassmeier, K.-H. 2005, JGR, 110, A12215
Narita, Y., Glassmeier, K.-H., Fornacon, K.-H., et al. 2006, JGR, 111, A01203
Ni, B., & Summers, D. 2010, PhPl, 17, 042903
Ogasawara, K., Livi, S. A., Mitchell, D. G., Armstrong, T. P., & Krupp, N. 2011, JGR, 116, A12207
Omura, Y., & Zhao, Q. 2012, JGR, 117, A08227
Omura, Y., & Zhao, Q. 2013, JGR, 118, 5008
Price, C. P., Swift, D. W., & Lee, L.-C. 1986, JGR, 91, 101
Pokhotelov, O. A., Sagdeev, R. Z., Balikhin, M. A., Onishchenko, O. G., & Fedun, V. N. 2008, JGR, 113, A04225
Remya, B., Reddy, R. V., Tsurutani, B. T., Lakhina, G. S., & Echer, E. 2013, JGR, 118, 785
Schwartz, S. J., Burgess, D., & Moses, J. J. 1996, AnGeo, 14, 1134

Sckopke, N., Paschmann, G., Brinca, A. L., Carlson, C. W., & Lühr, H. 1990, JGR, 95, 6337
Shoji, M., Omura, Y., & Lee, L. 2012, JGR, 117, A08208
Shoji, M., Omura, Y., Tsurutani, B. T., Verkhoglyadova, O. P., & Lembege, B. 2009, JGR, 114, A10203
Shprits, Y. Y., Chen, L., & Thorne, R. M. 2009, JGR, 114, A03219
Smith, E. J., & Tsurutani, B. T. 1976, JGR, 81, 2261
Sonnerup, B. U. O., & Cahill, L. J., Jr. 1967, JGR, 72, 171
Soucek, J., & Escoubet, C. P. 2011, AnGeo, 29, 1049
Soucek, J., Lucek, E., & Dandouras, I. 2008, JGR, 113, A04203
Southwood, D. J., Dougherty, M. K., Balogh, A., et al. 2001, JGR, 106, 30109
Summers, D., Thorne, R. M., & Xiao, F. 1998, JGR, 103, 20487
Tátrallyay, M., & Erdös, G. 2002, P&SS, 50, 593
Tátrallyay, M., & Erdös, G. 2005, P&SS, 53, 33
Thorne, R. M., & Kennel, C. F. 1971, JGR, 76, 4446
Treumann, R. A., Bostrom, R., LaBelle, J., & Sckopke, N. 1990, JGR, 95, 19099
Treumann, R. A., Georgescu, E., & Baumjohann, W. 2000, GeoRL, 27, 1843
Tsurutani, B. T., Arballo, J. K., Zhou, X.-Y., Galvan, C., & Chao, J. K. 2002a, in COSPAR Colloquia Series, ed. L.-H. Lyu (Oxford, UK: Pergamon Press), 97
Tsurutani, B. T., Dasgupta, B., Galvan, C., et al. 2002b, GeoRL, 29, 2233
Tsurutani, B. T., Echer, E., Richter, I., Koenders, C., & Glassmeier, K.-H. 2013, P&SS, 75, 17
Tsurutani, B. T., Falkowski, B. J., Verkhoglyadova, O. P., Pickett, J. S., Santolík, O., & Lakhina, G. S. 2011a, JGR, 116, A09210
Tsurutani, B. T., Gonzalez, W. D., Gonzalez, A. L. C., et al. 2006, JGR, 111, A07S01
Tsurutani, B. T., & Lakhina, G. S. 1997, Rev. Geophys., 35, 491
Tsurutani, B. T., Lakhina, G. S., Neubauer, F. M., & Glassmeier, K.-H. 1997, GeoRL, 24, 3129
Tsurutani, B. T., Lakhina, G. S., Verkhoglyadova, O. P., et al. 2011b, JGR, 116, A02103
Tsurutani, B. T., Page, D. E., Smith, E. J., et al. 1989, JGR, 94, 18
Tsurutani, B. T., Richardson, I. G., Lepping, R. P., et al. 1984, GeoRL, 11, 1102
Tsurutani, B. T., & Smith, E. J. 1986a, GeoRL, 13, 259
Tsurutani, B. T., & Smith, E. J. 1986b, GeoRL, 13, 263
Tsurutani, B. T., Smith, E. J., Anderson, R. R., et al. 1982, JGR, 87, 6060
Tsurutani, B. T., Smith, E. J., Burton, M. E., et al. 2001, JGR, 106, 30223
Tsurutani, B. T., Smith, E. J., & Jones, D. E. 1983, JGR, 88, 5645
Tsurutani, B. T., Thorne, R. M., Smith, E. J., Gosling, J. T., & Matsumoto, H. 1987, JGR, 92, 11074
Tsurutani, B. T., Verkhoglyadova, O. P., Lakhina, G. S., & Yagitani, S. 2009, JGR, 114, A03207
Vedenov, A. A., & Sagdeev, R. Z. 1958, Plasma Physics and the Problem of Controlled Thermonuclear Reactions, Vol. 3 (New York: Pergamon), 332
Verkhoglyadova, O. P., Tsurutani, B. T., & Lakhina, G. S. 2010, JGR, 115, A00F19
Zwan, B. J., & Wolf, R. A. 1976, JGR, 81, 1636